RadioGraphics

# Advancements in MR Imaging of the Prostate: From Diagnosis to Interventions[1]

TEACHING POINTS
See last page

*David Bonekamp, MD, PhD • Michael A. Jacobs, PhD • Riham El-Khouli, MD • Dan Stoianovici, PhD • Katarzyna J. Macura, MD, PhD*

Prostate cancer is the most frequently diagnosed cancer in males and the second leading cause of cancer-related death in men. Assessment of prostate cancer can be divided into detection, localization, and staging; accurate assessment is a prerequisite for optimal clinical management and therapy selection. Magnetic resonance (MR) imaging has been shown to be of particular help in localization and staging of prostate cancer. Traditional prostate MR imaging has been based on morphologic imaging with standard T1-weighted and T2-weighted sequences, which has limited accuracy. Recent advances include additional functional and physiologic MR imaging techniques (diffusion-weighted imaging, MR spectroscopy, and perfusion imaging), which allow extension of the obtainable information beyond anatomic assessment. Multiparametric MR imaging provides the highest accuracy in diagnosis and staging of prostate cancer. In addition, improvements in MR imaging hardware and software (3-T vs 1.5-T imaging) continue to improve spatial and temporal resolution and the signal-to-noise ratio of MR imaging examinations. Another recent advancement in the field is MR imaging guidance for targeted prostate biopsy, which is an alternative to the current standard of transrectal ultrasonography–guided systematic biopsy.



**CME FEATURE**

*See www.rsna.org/education/rg_cme.html*

**LEARNING OBJECTIVES FOR TEST 2**

*After reading this article and taking the test, the reader will be able to:*

- Describe the clinical background, prognosis, and current screening of prostate cancer.
- List the findings of prostate cancer at T1- and T2-weighted MR imaging and multiparametric MR imaging.
- Discuss the rationale for and technique of MR imaging–guided prostate biopsy.

**INVITED COMMENTARY**

*See discussion on this article by Oto (pp 704–706).*

**Abbreviations:** ADC = apparent diffusion coefficient, BPH = benign prostatic hyperplasia, DCE = dynamic contrast-enhanced, DRE = digital rectal examination, EES = extracellular-extravascular space, PSA = prostate-specific antigen, ROI = region of interest, SNR = signal-to-noise ratio, TKCM = tracer kinetic compartmental model

**RadioGraphics 2011;** 31:677–703 • **Published online** 10.1148/rg.313105139 • **Content Codes:** GU MR CT

[1]From the Russell H. Morgan Department of Radiology and Radiological Science, Johns Hopkins University School of Medicine, 601 N Caroline St, JHOC 3140C, Baltimore, MD 21287 (D.B., M.A.J., K.J.M.); Department of Radiology and Imaging Sciences, National Institutes of Health, Bethesda, Md (R.E.K.); and Robotics Program, Brady Urological Institute, Johns Hopkins University, Baltimore, Md (D.S.). Recipient of a Certificate of Merit award for an education exhibit at the 2009 RSNA Annual Meeting. Received May 20, 2010; revision requested July 19 and received September 13; accepted October 11. For this CME activity, the authors, editors, and reviewers have no relevant relationships to disclose. The authors discuss a robotic device for MR imaging–guided prostate biopsy that has not been approved by the FDA. **Address correspondence to** K.J.M. (e-mail: *kmacura@jhmi.edu*).

Supported in part by grants 1R01CA100184, P50 CA103175, P50CA88843, and U01CA070095 from the National Institutes of Health and an American Roentgen Ray Society Scholarship.

## Introduction

Prostate cancer is the most frequently diagnosed cancer in males, accounting for 25% of all cancers in males (192,280 of 766,130 newly diagnosed cancers in males in 2009), compared with 15% for lung cancer. It is the second leading cause of cancer-related death in men, making up 9% of cancer deaths in males (27,360 of 292,540 cancer-related deaths in males in 2009), a value exceeded only by the death rate from lung cancer in males (30%). Sixteen percent of males (one in six) will develop prostate cancer during their lifetime (1).

The prevalence of prostate cancer increases with age; 34% of men in the 5th decade of life and up to 70% aged 80 years or older have histologic evidence of prostate cancer. The anticipated demographic change in an aging population is expected to increase the incidence of prostate cancer. Over the past 25 years, the 5-year survival rate for all stages of prostate cancer combined has increased from 69% to almost 99%. The corresponding 10-year survival rate is 93%, and the 15-year survival rate is 79%. The notable improvements in survival, particularly at 5 years, are commonly attributed to earlier diagnosis and improvements in treatment.

Radical treatment options for patients with prostate cancer include prostatectomy (for organ-confined T1 and T2 disease) and hormone ablation and radiation therapy (for advanced extraprostatic T3 and T4 disease). Local and minimally invasive therapy choices for organ-confined prostate cancer include cryoablation, radiofrequency ablation, brachytherapy, photodynamic therapy, and high-intensity focused ultrasonography (US); however, these therapies require exact localization of the cancer. In certain situations, expectant management (watchful waiting) is a legitimate choice for patients with small-volume, low-grade, low-risk disease without any additional morbidity.

With accurate staging and localization of prostate cancer, minimally invasive therapies can provide uncompromised oncologic outcome with significantly less comorbidity. However, patient selection for such treatments remains a challenge, since the tumor biology of prostate cancer still remains poorly understood. Most patients in whom prostate cancer is diagnosed die *with* the disease rather than *of* the disease.

Although several methods have been developed to predict patients' outcome (2), it is still difficult to project which patients will experience progression of the disease. The most important predictors of prognosis in prostate cancer are the Gleason score and the clinical stage at the time of diagnosis. Prostate-specific antigen (PSA) screening has led to earlier diagnosis of tumors at lower clinical stages and with lower Gleason scores (3).

Despite PSA screening, there remains a major medical and socioeconomic impact due to morbidity and mortality from prostate cancer. The three dimensions in the accurate assessment of prostate cancer are detection, localization, and staging. Improvements in all three of these dimensions are prerequisites for optimal clinical management and therapy selection.

Magnetic resonance (MR) imaging continues to evolve as a powerful modality for localization and staging of prostate cancer. Recent advances employ functional and physiologic MR imaging techniques, in addition to the established morphologic imaging with T1-weighted and T2-weighted sequences. Often, these new techniques are used together in a multiparametric approach.

Diffusion-weighted imaging interrogates the tissue microstructure at the microscopic scale of water self-diffusion (Brownian motion). MR spectroscopy probes the concentration of biochemical disease markers in tissues. Dynamic contrast material–enhanced (DCE) MR imaging dynamically captures the distribution of intravenously administered gadolinium-based contrast agents between tissue and the blood pool, allowing characterization of alterations in the microvascular environment resulting from tumor angiogenesis. All of these techniques benefit from continuing improvements in imaging unit hardware and software. MR-compatible devices have been developed for diagnostic and therapeutic interventions and for minimally invasive procedures.

In this article, we review the currently available MR methodologies for the evaluation of prostate cancer in a practical and integrated clinical context and discuss and illustrate the recent advancements in the field, including MR imaging guidance for targeted prostate biopsy as an alternative to transrectal US–guided systematic biopsy, which is the current standard. We also discuss the advantages and limitations of current diagnostic MR imaging of the prostate. In addition, we provide a comparison of prostate MR imaging at 3 T and 1.5 T. Finally, development of an imaging algorithm for MR imaging of the prostate is described.

## Clinical Background and Specific MR Imaging Considerations

### Prostate Cancer Screening

Teaching Point

Currently, prostate cancer screening is based on assessment of the level of PSA elevation and results of digital rectal examination (DRE). Both markers have suboptimal accuracy for the diagnosis of prostate cancer. DRE is affected by interexaminer variability, irrespective of experience, and is limited to assessment of peripheral zone tumors. DRE remains a fundamental part of screening owing to its being part of the clinical examination without additional cost, its ubiquitous availability, and its ability to allow identification of the tumor in 14% of men with prostate cancer (4).

PSA screening was recognized as a screening tool in 1991 after its initial description in 1979. Its introduction has led to a significant decrease in stage at diagnosis and to detection of tumors of very small volume (often <0.5 $cm^3$) and of low Gleason score (≤6). Despite a diagnosis of prostate cancer, patients with such small and low-grade cancers may not be subject to decreased life expectancy. This is also suggested by the discrepancy between a patient's lifetime risk of a prostate cancer diagnosis (16.7%) and the risk of death from the disease (3%–4%). Therefore, clinically significant prostate cancer has been defined as a tumor with a volume greater than 0.5 $cm^3$ and a Gleason score greater than or equal to 7 (5).

Despite its significant impact, PSA screening is not optimal. PSA screening has been criticized due to its relatively poor sensitivity and specificity. For PSA levels under 10 ng/mL, elevation above the threshold of 4 ng/mL (values above this threshold are commonly regarded as abnormal) has low specificity for prostate cancer. In 70%–80% of patients with mild elevation of PSA level, the increased PSA level is in fact caused by benign conditions such as benign prostatic hyperplasia (BPH) or prostatitis, resulting in a false-positive PSA test result and subsequently in an unnecessary biopsy.

At least 15% and up to 44% of biopsy-proved prostate cancers occur in patients with PSA levels in the accepted normal range below 4 ng/mL (3). In 15.2% of prostate cancer patients with a normal PSA level, the tumor is not palpable and therefore is clinically silent (3). Nevertheless, these clinically silent tumors may significantly affect the patients' life expectancy, since 15.6% of these cancers are found to be high grade (Gleason score of 7–9) (3). At PSA levels of 2–10 ng/mL, more than one-third of prostate cancers occur at very low total PSA levels of 2–3.9 ng/mL (6). These low PSA level cancers were found in younger patients and at lower stages with a smaller prostate volume.

In addition to the total PSA level, several additional PSA level–based indexes are clinically used today due to their ability to stratify patients into different risk groups. PSA velocity is the increase in total PSA level over time, which can also be expressed as the PSA doubling time. A PSA velocity of greater than 0.4–0.75 ng/mL/y is commonly considered suspicious for the presence of prostate cancer.

Different molecular forms of total PSA have been identified, for example, free PSA and PSA bound to $\alpha_1$-antichymotrypsin. PSA in serum is predominantly complexed to protease inhibitors; however, in the form of free PSA it is not bound to these proteins. Use of the percentage of free PSA—that is, the ratio of free PSA to total PSA—has been found to improve the specificity of an elevated total PSA level. In benign processes of the prostate, the percentage of free PSA tends to be higher in comparison to the total PSA. Use of the percentage of free PSA for screening is often recommended in the setting of a normal DRE result together with a total PSA level of 4.0–10 ng/mL. At times, screening with the percentage of free PSA is initiated when a high normal PSA level is found.

In the setting of a high normal total PSA level of 2.0–3.9 ng/mL or in the intermediate range of 4.0–10 ng/mL, data suggest that a free PSA level above 18% of the total PSA is associated with a risk of less than 10% for prostate cancer; conversely, a free PSA level below 10% is associated with a 30% risk for prostate cancer (7). Accordingly, in the setting of a low to intermediate total PSA level, the clinical decision to perform a prostate biopsy is often made if the free PSA level is found to be below 20%–25%. Additional free PSA subforms exist, including precursor PSA, "benign" PSA, and intact PSA, which may help increase the specificity of the percentage of free PSA; however, these subforms are beyond the scope of this article.

The PSA density is defined as the total PSA level divided by the prostate volume in cubic centimeters (classically as measured at transrectal

US). PSA density is based on the concept that prostate cancer produces more PSA per gram of tissue than does normal or benign tissue. Its clinical usefulness is controversial due to limitations in specificity and sensitivity. Although a PSA density greater than or equal to 0.15 was proposed as the threshold for biopsy in men with PSA levels of 4–10 ng/mL, approximately 40% of prostate cancers were missed with this approach. However, the most significant barrier to its widespread use is the unwillingness of patients and physicians to have transrectal US performed without a biopsy.

## Transrectal US and Guided Biopsy

US is widely used in the form of transrectal US, nearly always with the primary intent for transrectal biopsy to be performed in the same session.

Transrectal US alone is not recommended for initial screening (eg, according to the current screening guidelines of the American Cancer Society and the Centers for Disease Control and Prevention) owing to *(a)* lack of supportive data on sufficient specificity or ability to significantly increase the detection rate of prostate cancer and *(b)* its significant cost when used as a screening tool. Transrectal US is mainly used to provide visual guidance for biopsy.

At transrectal US, most prostate cancers (60%–70%) are hypoechoic to the normal peripheral zone, whereas up to 40% of lesions are not distinguished from the background normal parenchyma owing to its isoechogenicity (8). Evaluation of the transition zone with transrectal US is very limited. In a large study, transrectal US was found to have only a 15.2% positive predictive value in detection of cancers versus 28% for DRE; therefore, both techniques are unable to allow differentiation of an abundance of benign processes mimicking prostate cancer from true-positive cases. Transrectal US used in the absence of palpable findings has a low sensitivity of 30%–45%, meaning that less than one-half of the ultimately diagnosed cancers can be visualized with transrectal US, even if the improved systematic sextant approach is used (9).

If no abnormality is visualized at US, transrectal US provides anatomic landmarks for systematic biopsy (eg, with the sextant or octant sampling scheme). Transrectal US–guided prostate needle biopsy is performed in men with an abnormal DRE result, an elevated PSA level (>4.0 ng/mL), and a PSA velocity greater than 0.4–0.75 ng/mL/y, as well as in men in whom a previous biopsy showed high-grade prostatic intraepithelial neoplasia or atypia (repeat biopsy is usually performed 3–12 months after the initial biopsy). Some centers perform transrectal US–guided biopsy in the setting of age-specific elevation of PSA level, a low percentage of free PSA (eg, <22%–25%), or a PSA density greater than 0.15. The estimated number of prostate biopsies performed yearly in the United States is 1,300,000. In 2007, these resulted in detection of 186,320 new cases of prostate cancer (10).

As a confirmatory test for patients suspected of having prostate cancer on the basis of DRE result and PSA level, transrectal US–guided biopsy provides a sufficiently high specificity for diagnosis; however, it has limited sensitivity. With prostate biopsy, cancer is missed in up to 10%–38% of men eventually found to have prostate cancer (11), and not uncommonly patients require repeat biopsies until a diagnosis is made. In some instances, failure rates may be as high as 73%. For example, the prostatic apex is difficult to access during biopsy, and lateral as well as anterior cancers are not well evaluated with standard sextant biopsies (11).

The management of cases in which a first set of biopsies was negative for cancer is a known problem and creates uncertainty and emotional stress for the patients, who may be facing a series of repeat biopsies, with cancer detection rates of 34%, 25%, 24%, and 21% for the first, second, third, and fourth biopsies, respectively, as shown in a recent study of 10,429 biopsies (12). Moreover, with the current stage migration, the smaller tumors are becoming ever more difficult to sample. The total volume of the cores extracted in a biopsy session is very small in comparison with the gland volume, less than 1%. Therefore, the overall probability of sampling a minute cancer in the early stage is low and is even lower for larger prostate volumes.

Options in patients with prior negative biopsy results and a high suspicion for prostate cancer

include saturation biopsy and transperineal biopsy. During a saturation biopsy, a much larger number of cores (not uncommonly 40–80) is obtained. Different sampling schemes including saturation biopsy may be performed transperineally, allowing better access to the prostatic apex; however, decreased access to the prostatic base has been described. Transperineal biopsy has been found to be associated with no significant increased risk for complications when compared with transrectal biopsy (13). Although transperineal and transrectal biopsies have been found to have comparable sensitivity, transrectal biopsy remains markedly more popular at this time, an outcome attributed to the increased technical difficulty and the need for at least local anesthesia with transperineal biopsy.

Intraglandular anatomic localization of prostate cancer with transrectal US–guided biopsy has been found to often be inaccurate when compared with the final prostatectomy results; this outcome is likely caused by difficulty in sampling the correct anatomic location for each needle pass. Without accurate intraglandular tumor localization, the patient may not be able to consider minimally invasive local therapies that can improve the quality of life with a good oncologic outcome.

## Role of MR Imaging in Screening, Localization, and Biopsy

Because of the limitations of DRE, transrectal US, and transrectal US–guided biopsy, there is a need for further imaging, with MR imaging being an attractive modality owing to its high resolution and soft-tissue contrast. As cases in which MR imaging will be the only modality to demonstrate a suspicious focus are unavoidable, biopsy guidance with MR imaging continues to be developed.

As for localization of prostate cancer, PSA screening provides no spatial information and DRE essentially involves a surface assessment of the prostate. DRE and transrectal US are also operator dependent. Prostate cancer is multifocal in 85% of cases, and this property can be assessed only with imaging or biopsy, not with PSA screening; DRE has only very limited capability for this purpose. MR imaging is currently best suited for detection of multiple foci and for localization of prostate cancer, which is becoming increasingly important.

## Staging of Prostate Cancer

Results of clinical staging with DRE, serum PSA levels, and biopsy-derived Gleason score are of limited use in guiding treatment decisions. With clinical staging, prostate cancer stage is underestimated in 30%–60% of cases; however, this is an inexpensive and specific technique in clearly advanced disease, in that once clinical staging suggests inoperability, the risk for inappropriate exclusion of patients from indicated surgery is relatively low. However, patients with clinically understaged disease may undergo unnecessary surgery.

Therefore, MR imaging and other imaging modalities have been evaluated for their ability to improve staging accuracy. The most important aspect of local staging is differentiation between organ-confined disease (stage T1 or T2) and early advanced disease in the form of extracapsular extension or seminal vesicle invasion (stage T3). Advanced MR imaging techniques have been repeatedly shown to be more accurate in differentiation between stage T2 and T3 prostate cancer than other imaging modalities and are preferred for local staging, despite the lack of clearly specified clinical protocols for integration of MR imaging at this time.

Of all noninvasive anatomic imaging modalities, MR imaging is most suited for evaluation of the prostate, as it has unparalleled ability to depict detail of the prostate owing to its exquisite soft-tissue contrast. Computed tomography (CT) does not provide sufficient soft-tissue contrast beyond size assessment of the prostate. Although CT is valuable in the evaluation of pelvic lymphadenopathy and bone metastases, MR imaging and bone scanning have been found superior in their assessment (14).

Currently experimental or reserved to few institutions is use of fluorine 18 ($^{18}$F)–labeled radiotracers (eg, $^{18}$F fluoroethylcholine) for positron emission tomography for staging prostate cancer. Use of ultrasmall paramagnetic iron oxide particles with MR imaging has been found to allow detection of nearly 100% of pathologically involved lymph nodes (15). Single photon emission computed tomography (SPECT) with indium 111 ($^{111}$In)–labeled murine monoclonal antibody to prostate-specific membrane antigen (capromab pendetide) is hampered by limited image resolution and limited specificity (16).

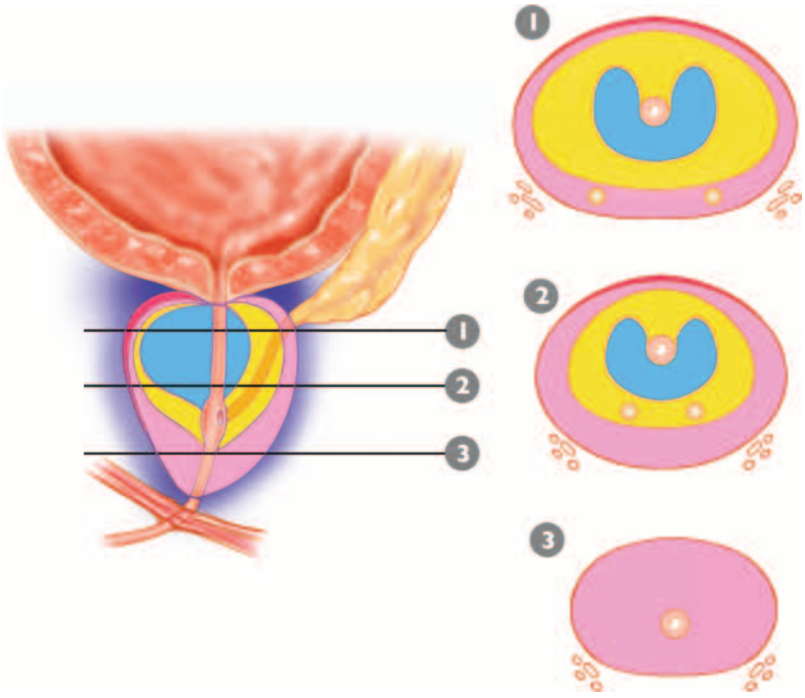


**Figure 1.** Distribution and proportions of the tissue layers composing the prostate. Diagram of the prostate shows its zonal anatomy in the sagittal plane and corresponding axial sections from the base *(1)*, midgland *(2)*, and apex *(3)*. Note the anterior fibromuscular stroma (red), peripheral zone (pink), central zone (yellow), and transition zone (blue).

## Anatomy, Histologic Features, and Morphologic Imaging of the Prostate

### Imaging Anatomy of the Prostate

Anatomically, the prostate is divided from superior to inferior into the base (just below the urinary bladder), the midgland, and the apex (Figs 1, 2). In the axial plane, the prostate is divided into four zones: *(a)* the anterior fibromuscular stroma, which contains no glandular tissue; *(b)* the transition zone surrounding the urethra, which contains 5% of the glandular tissue; *(c)* the central zone, which contains 20% of the glandular tissue; and *(d)* the outer peripheral zone, which contains 70%–80% of the glandular tissue (17). The volume of the peripheral zone increases from the base to the apex of the gland.

Teaching Point

Ninety-five percent of prostate cancers are adenocarcinomas that develop from the acini of the prostatic ducts. Thus, prostate cancers arise in the glandular tissue, with about 70% originating in the peripheral zone, 25% in the transition zone, and 5% in the central zone. At imaging, the transition zone cannot be separated from the central zone; therefore, these two zones are often referred to together as the central gland (Fig 2).

The prostate does not have a true capsule, only an outer band of concentric fibromuscular tissue that is an inseparable component of the prostatic stroma (18). The outer-layer "capsule" is most apparent posteriorly and posterolaterally; it is seen at MR imaging as a thin layer of tissue that is dark on T2-weighted images. The capsule is an important landmark for assessment of extraprostatic tumor extension, since irregularities, bulges, and disruptions of the capsule are signs of tumor invasion or spread outside the confines of the prostate.

The periprostatic neurovascular bundles course posterolateral to the prostate bilaterally. They are well seen at imaging at the 5-o'clock and 7-o'clock positions in reference to the prostate (Fig 2). At the apex and base, the nerve bundles send penetrating branches through the capsule, which provide a route for extraprostatic tumor extension.

### Grading of Prostate Cancer with the Gleason System

Histologic evaluation of the prostate is performed by using the Gleason grading system (19). Tumors are assigned a primary grade, which is based on the predominant pattern of tissue differentiation, and a secondary grade, which based on the second most common pattern of tissue differentiation. The two numbers (primary grade and secondary grade) are added to produce the final Gleason score.

A tumor with a Gleason score of 6 will have components of Gleason grade 3 + Gleason grade 3. A tumor with a Gleason score of 7 can have components of Gleason grade 3 + Gleason grade 4 or of Gleason grade 4 + Gleason grade 3. The biologic behavior of a tumor with a Gleason score

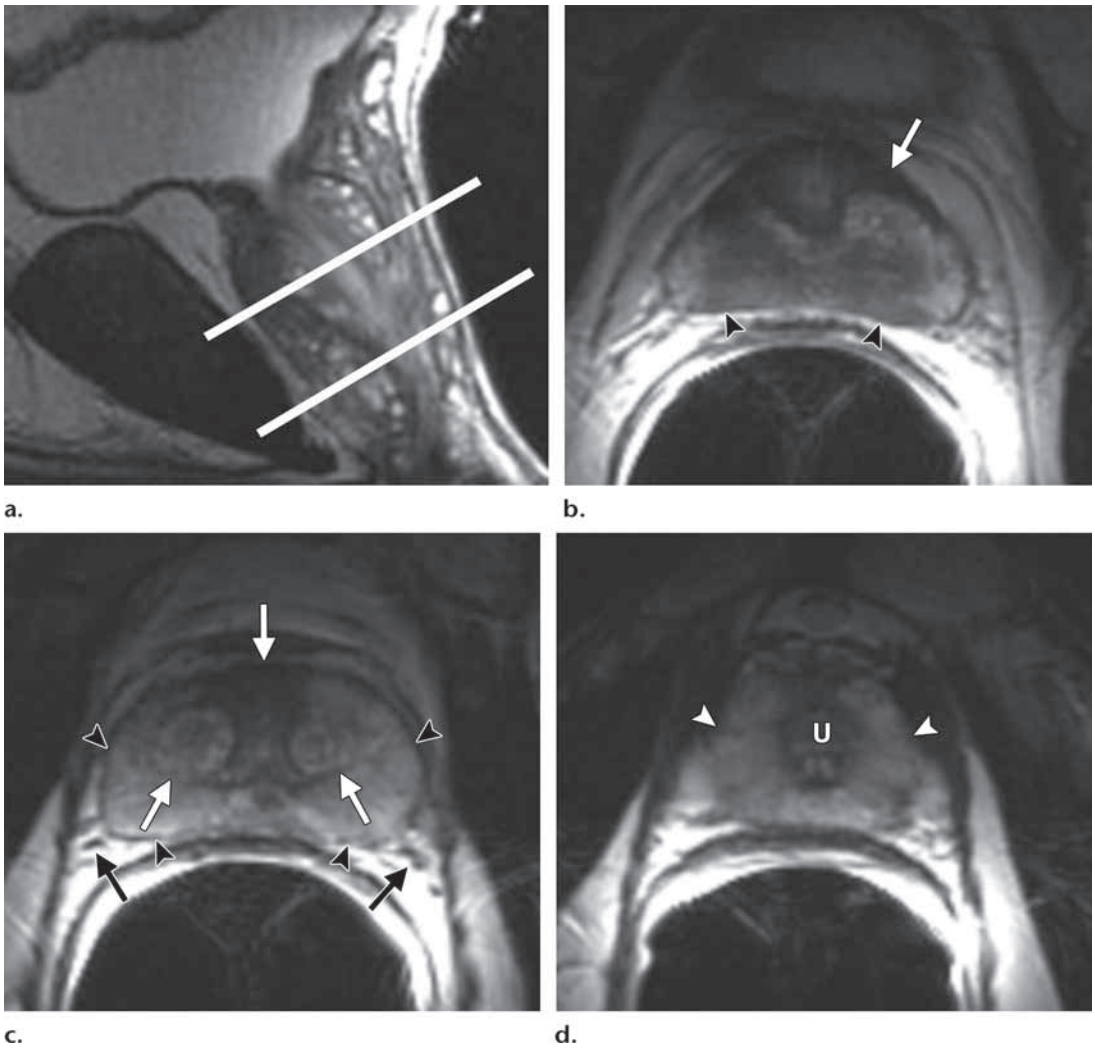


**Figure 2.** Anatomy of the prostate on endorectal MR images obtained at 1.5 T. **(a)** Sagittal T2-weighted image (repetition time msec/echo time msec = 3350/92) shows division of the prostate into three sections in the craniocaudal direction. The superior one-third of the prostate below the bladder is the base. The middle one-third is the midgland. The distal one-third is the apex. **(b)** Axial T2-weighted image (6000/92) shows the base of the prostate. The anterior fibromuscular stroma (arrow) consists of nonglandular tissue and appears dark. Note the symmetric homogeneous muscular stroma layer (arrowheads) in the posterior prostate base. **(c)** Axial T2-weighted image of the midprostate shows the homogeneously bright peripheral zone (arrowheads) surrounding the central gland (white arrows). The central gland is composed of the transition zone and central zone, which cannot be resolved at imaging. Therefore, they are referred to jointly as the *central gland*. Note the neurovascular bundles at the 5-o'clock and 7-o'clock positions (black arrows). **(d)** Axial T2-weighted image of the prostatic apex shows the homogeneous peripheral zone (arrowheads) surrounding the urethra *(U)*. Note that the volume of the peripheral zone increases from the base to the apex.

of 4 + 3 would be more aggressive than that of one with a Gleason score of 3 + 4 (20,21).

In the United States, the lowest Gleason score for cancer is a Gleason score of 6; such a tumor is considered well differentiated and has a good prognosis. Tumors with Gleason scores of 8–10 have the worst prognosis and the highest risk for recurrence. Tumors with a Gleason score of 7 have a variable prognosis and an intermediate risk of recurrence (21).

## Morphologic Imaging with T2-weighted and T1-weighted Sequences

On T2-weighted images, the normal peripheral zone has homogeneous high signal intensity and the central gland has variable amounts of intermediate signal intensity, which is often replaced by well-circumscribed hyperplastic nodules of BPH (Fig 3).

**Figure 3.** BPH on endorectal MR images obtained at 1.5 T. **(a)** Axial T2-weighted image (6000/92) shows well-defined heterogeneously bright hyperplastic nodules in the central prostate. Note the discrete dark margins of the junction of the central gland and the peripheral zone pseudocapsule (arrows). **(b)** Color map from computer-assisted diagnosis analysis of DCE MR imaging data shows a region of interest (ROI) marking the left hyperplastic nodule of BPH. **(c)** Permeability histogram shows a wide range of permeability values for tissue in the ROI. **(d)** Kinetic curve (percentage of enhancement over time) from DCE MR imaging data shows a washout pattern of enhancement in the BPH tissue included in the ROI. In this case, the morphologic features at T2-weighted imaging are more specific for the diagnosis of BPH than are the results of kinetic curve analysis, which may suggest malignancy. **(e)** Image from MR spectroscopy shows a voxel grid overlay over the T2-weighted image (left); the spectral display (right) shows normal spectra in the region of BPH. For example, the spectrum for the selected voxel (arrow) shows a high citrate *(Ci)* peak and a low choline *(Ch)* peak in the benign tissue of BPH. Ch + Cr/Ci = 0.297, where *Cr* = creatine.

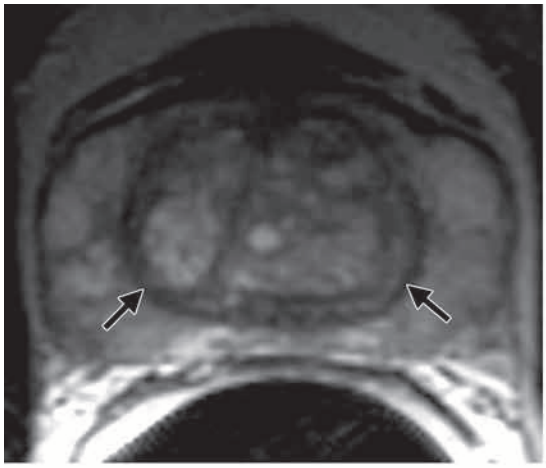

a.

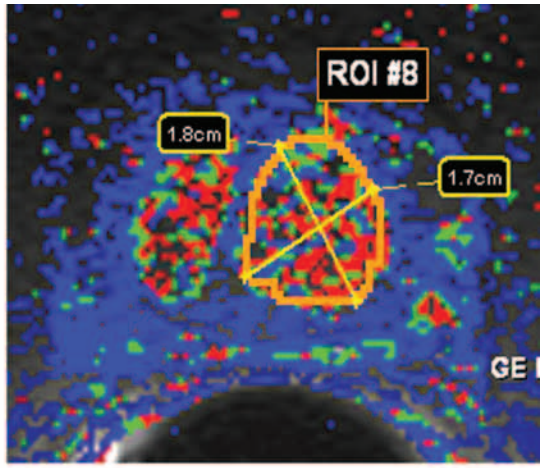


b.

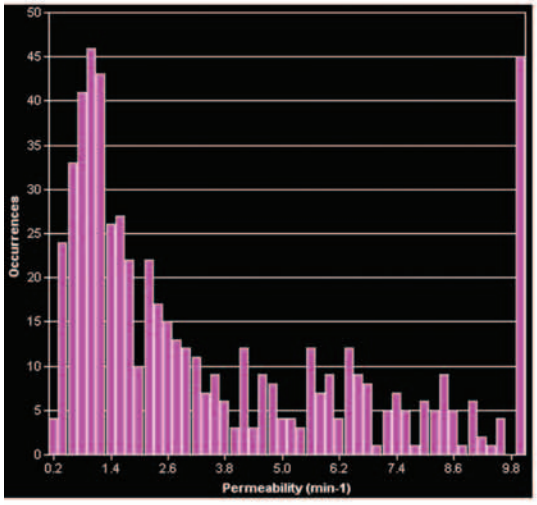


c.

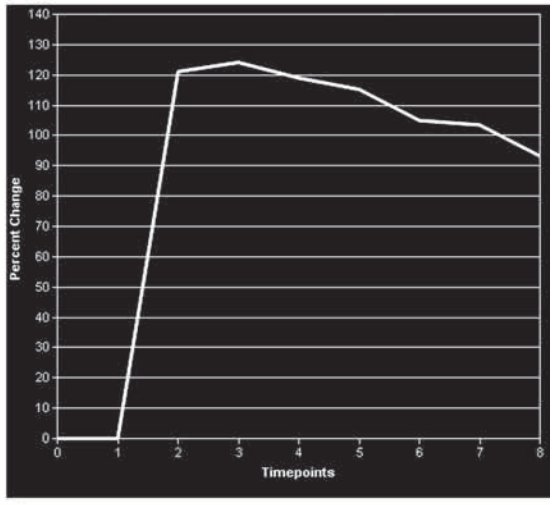


d.

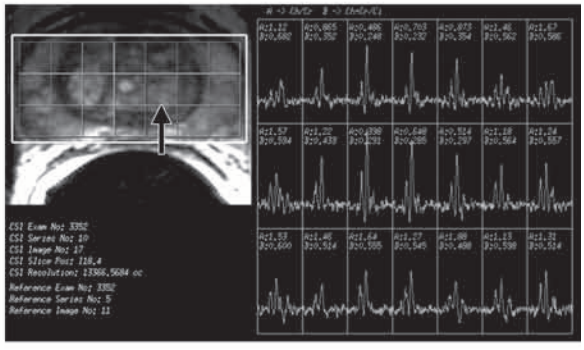

e.

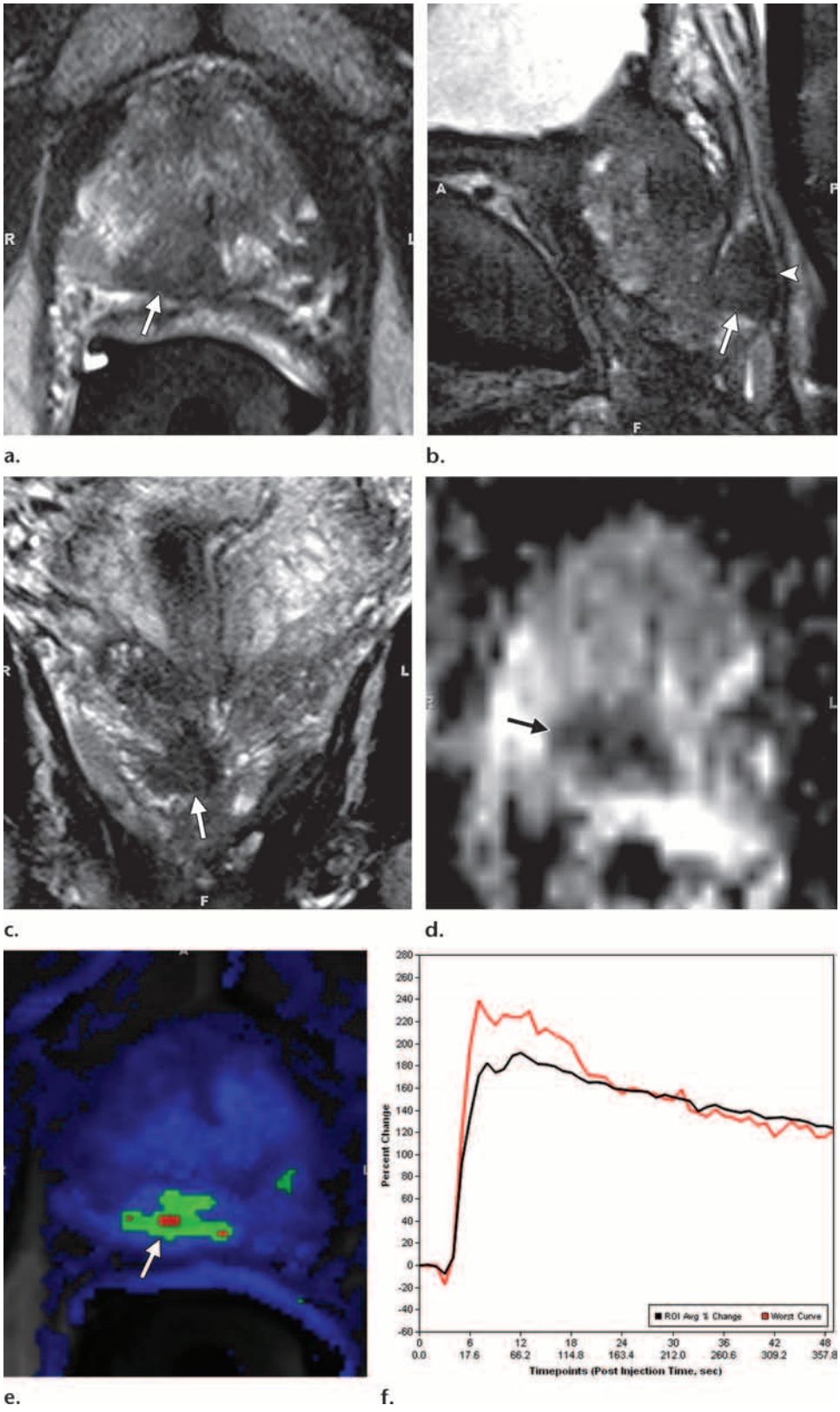


**Figure 4.** Prostate cancer in a 72-year-old man with a Gleason score of 4 + 3 and a PSA level of 7.2 ng/mL. Endorectal MR imaging of the prostate was performed at 3.0 T. **(a)** Axial T2-weighted image (5000/123) of the prostatic apex shows a hypointense nodule (arrow) in the right side of the apex. **(b)** Sagittal T2-weighted image (5000/153) shows the dark nodule in the prostatic apex (arrow). Note the intact, well-defined, thin, dark prostatic capsule (arrowhead). **(c)** Coronal T2-weighted image (3360/153) shows the hypointense spiculated nodule (arrow). This is a typical morphology for prostate cancer. **(d)** Axial apparent diffusion coefficient (ADC) map from diffusion-weighted imaging shows restricted diffusion (ADC = 0.7 × $10^{-3}$ $mm^2$/sec) in the region of malignancy (arrow). **(e)** Color map from DCE MR imaging shows that the area of highest permeability (arrow) is in the region of prostate cancer, a finding that corresponds to the findings on the T2-weighted images and the ADC map. **(f)** Kinetic curve (percentage of enhancement over time) from DCE MR imaging shows a washout pattern of enhancement, typical of malignancy, in the prostatic apex nodule.

A series of studies in the late 1980s established that prostate cancer is characterized by low T2 signal intensity replacing the normally high T2 signal intensity in the peripheral zone (Fig 4) (22). However, the presence of decreased T2 signal intensity in the peripheral zone is of limited sensitivity because some prostate tumors are isointense (Fig 5). This finding is also of limited

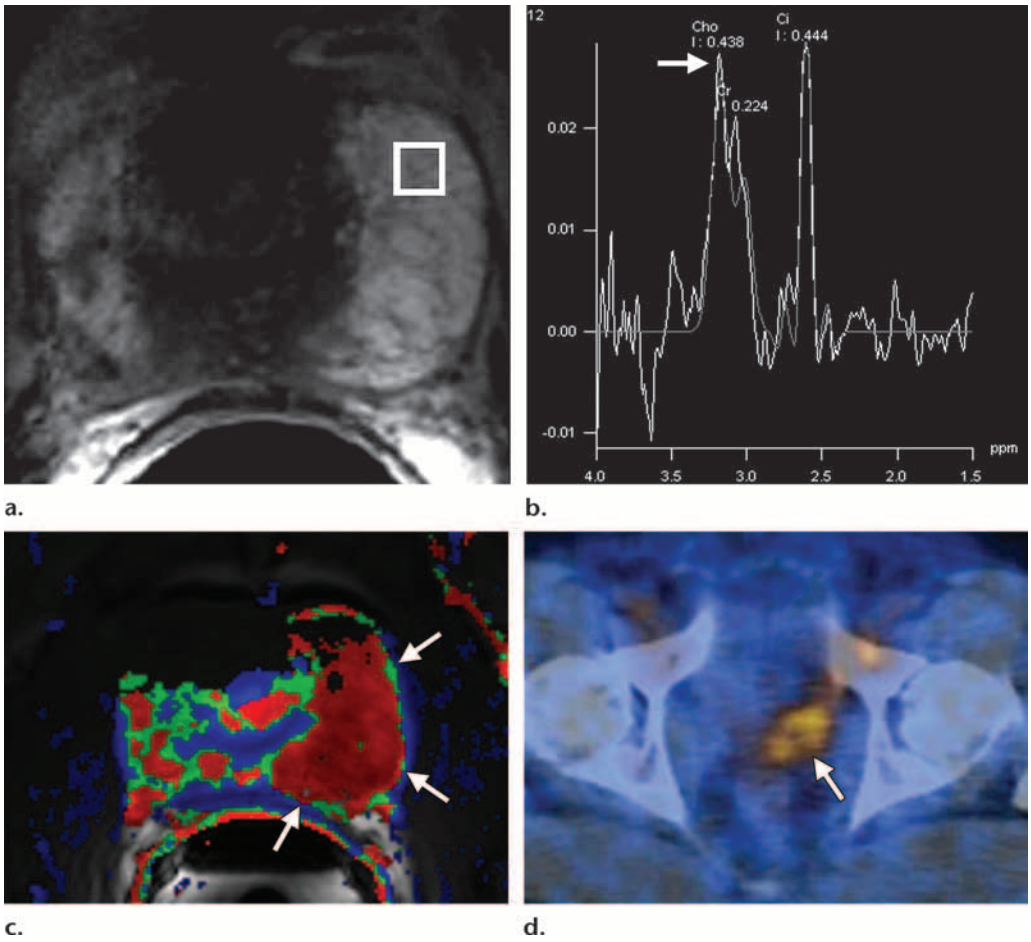


**Figure 5.** Prostate cancer in a 43-year-old man with a Gleason score of 4 + 3 and a PSA level of 90.5 ng/mL. Endorectal MR imaging was performed at 3.0 T. **(a)** T2-weighted image (4860/109) shows a voxel of interest (square) in the left peripheral zone. Although the left peripheral zone is enlarged compared with the right peripheral zone, it has no focal dark areas. There are patchy dark abnormalities in the right peripheral zone. **(b)** MR spectroscopic spectrum from the voxel of interest shows a markedly elevated level of choline *(Cho)* (arrow) that is almost equal to the citrate *(Ci)* peak. Elevation of choline level with a decrease in citrate level is the spectral signature of prostate cancer. *Cr* = creatine. **(c)** Color DCE MR map shows a large area of high permeability ($K^{trans}$) occupying the entire left peripheral zone (arrows). **(d)** Axial image from a SPECT study with $^{111}$In-labeled prostate monoclonal antibody (capromab pendetide [ProstaScint; Cytogen, Princeton, NJ]) shows avid uptake in the entire left prostate (arrow), a finding compatible with a large-volume prostate cancer. As seen in this case, some aggressive prostate cancers, even of large volume, may appear isointense on T2-weighted images; thus, morphologic imaging alone may not be able to show these tumors. Functional MR imaging—MR spectroscopy and DCE MR imaging—as well as antibody imaging accurately depicted this large prostate cancer.

specificity because there are other possible causes of low T2 signal intensity in the peripheral zone, including hemorrhage, prostatitis, scarring, atrophy, and effects of radiation therapy, cryosurgery, or hormonal therapy.

Prostate cancer arising in the transition zone poses additional imaging difficulties because of the heterogeneity of signal intensity in the central gland. Although there are several findings supporting the diagnosis of a transition zone tumor (23), such as a region of homogeneous low T2 signal intensity in the transition zone (Fig 6) and lack

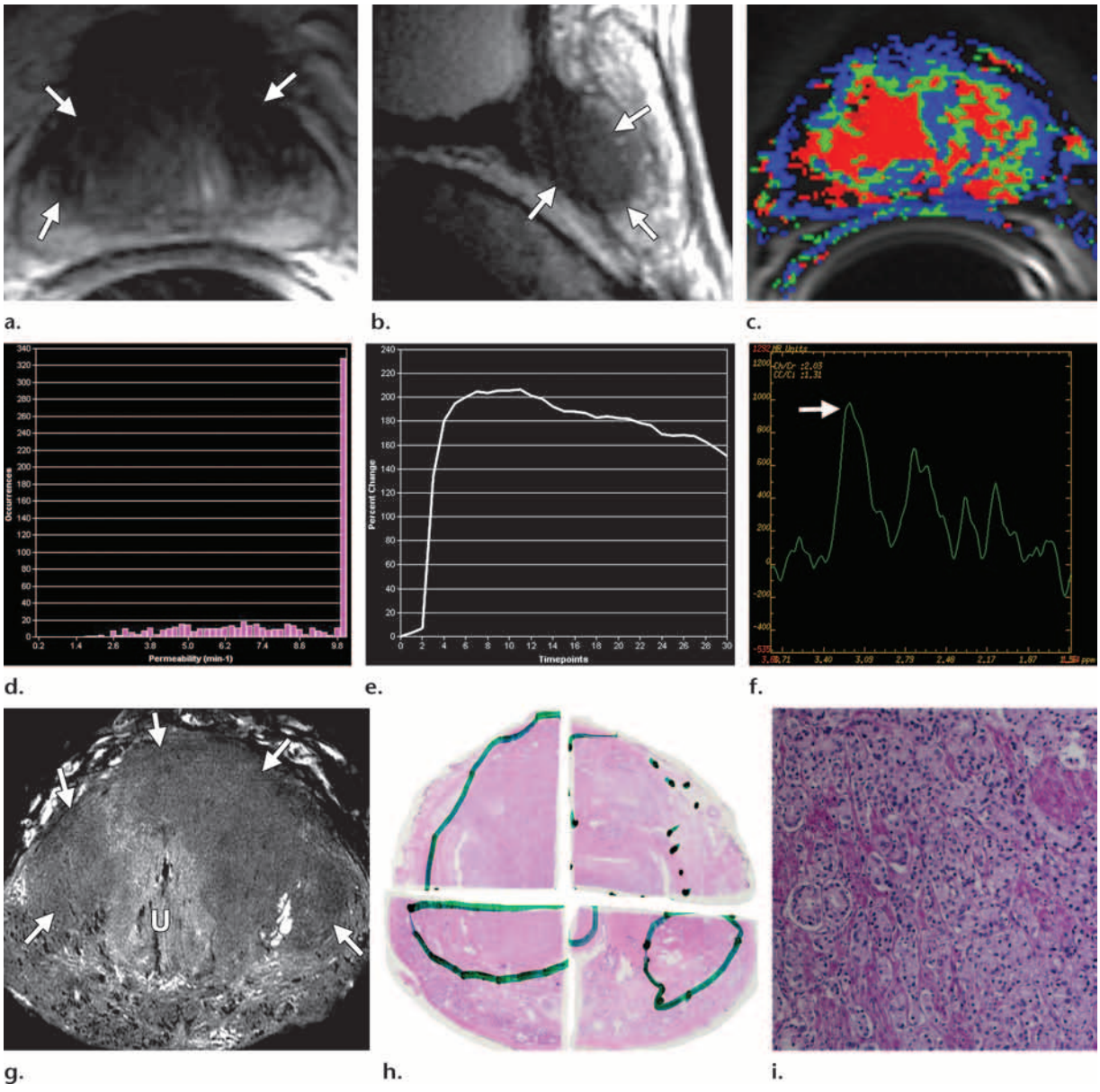


**Figure 6.** Prostate cancer of the transition zone in a 52-year-old man with a Gleason score of 3 + 4 and a PSA level of 19 ng/mL. Endorectal MR imaging was performed at 1.5 T. **(a)** Axial T2-weighted image (6000/92) shows ill-defined homogeneous dark infiltration of the central gland (arrows). **(b)** Sagittal T2-weighted image (3350/92) shows homogeneous dark tissue replacing the central gland (arrows). **(c)** Axial color DCE MR map shows a large area of high permeability ($K^{trans}$) (red areas) in the transition zone. **(d)** Permeability histogram shows a shift toward high permeability values, a finding characteristic of cancer. **(e)** Kinetic curve (percentage of enhancement over time) shows typical washout pattern in the transition zone tumor. **(f)** MR spectroscopic spectrum from the transition zone tumor shows a high choline *(Cho)* peak (arrow) at 3.2 ppm that is above that of citrate *(Ci)* at 2.64 ppm. Cho + Cr/Ci = 1.31, where *Cr* = creatine; this value is typical of prostate cancer. **(g)** Ex vivo T2-weighted image (4700/42) of the specimen, obtained at 9.4 T, shows highly cellular, compact dark tissue in the central gland (arrows) surrounding the urethra *(U)*. **(h)** Photograph of a whole-mount reconstructed histologic section (original magnification, ×2; hematoxylin-eosin [H-E] stain) of the midgland shows a large volume of tumor in the transition zone (outlined in green). Note the excellent correlation with the ex vivo image in **g** and the in vivo image in **c**, which show cancer of high cellular density in the transition zone. **(i)** Photomicrograph of a histologic section (original magnification, ×40; H-E stain) from the transition zone tumor shows loss of gland units and sheets of cancer cells with randomly scattered lumina. Note the muscular stroma component between the tumor cells.

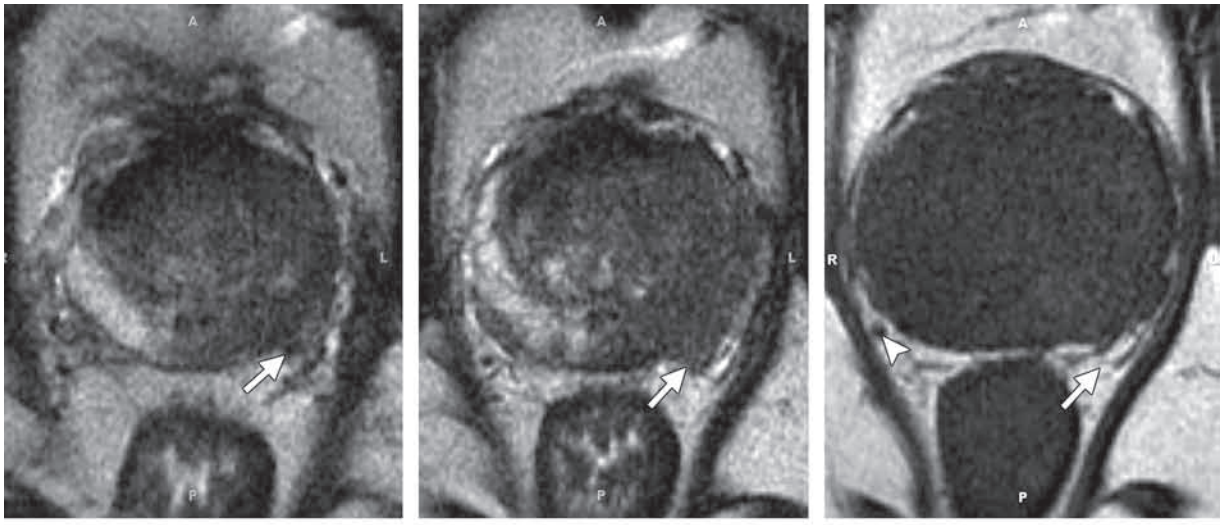


a. b. c.

**Figure 7.** Prostate cancer in a 51-year-old man with a Gleason score of 3 + 3 and a PSA level of 36.4 ng/mL. MR imaging of the prostate was performed at 3.0 T with a body matrix coil. **(a)** Axial T2-weighted image (4000/109) at the level of the prostate base shows confluent dark signal intensity replacing a large volume of the left peripheral zone, with extraprostatic tumor extension (arrow) involving the left neurovascular bundle. **(b)** Axial T2-weighted image at the level of the midgland shows the extracapsular extension of the tumor, with encasement of the left neurovascular bundle (arrow). **(c)** Axial T1-weighted image (600/11) shows good definition of the prostatic contour and the extracapsular tumor extension on the left into the bright periprostatic fat. Note the obliterated left neurovascular bundle (arrow) in comparison with the intact right neurovascular bundle (arrowhead).

of the low-signal-intensity rim commonly seen in association with BPH (Fig 3), low signal intensity is also normally seen in the anterior fibromuscular stroma (Fig 2) as well as in the stromal type of BPH. Several studies that investigated the accuracy of MR imaging in detection of prostate cancer reported low sensitivity, low specificity, and high interobserver variability, even when high-resolution endorectal MR imaging was used.

T1-weighted imaging of the prostate is of limited use for assessment of prostate morphology, as detail of the prostate is not well seen. T1-weighted sequences are mainly used *(a)* for detection of postbiopsy hemorrhage; *(b)* for evaluation of the contour of the prostate and the status of the neurovascular bundles, which are well seen in the bright periprostatic fat (Fig 7); and *(c)* as a baseline sequence for calculation of precontrast T1-weighted and DCE images for purposes of subtraction.

## Staging of Prostate Cancer with Morphologic Imaging

MR imaging criteria for organ-confined versus extraglandular tumor invasion, in the form of extracapsular tumor extension and seminal vesicle invasion, have been established. At endorectal MR imaging, criteria for extracapsular extension include asymmetry of the neurovascular bundle, tumor encasement of the neurovascular bundle, a bulging prostatic contour, an irregular or spiculated margin, obliteration of the rectoprostatic angle, capsular retraction, a tumor-capsule interface of greater than 1 cm, and a breach of the capsule with evidence of direct tumor extension (Fig 7) (23).

At multivariate feature analysis, the following MR imaging criteria were most predictive of extracapsular extension: a focal irregular capsular bulge, asymmetry or invasion of the neurovascular bundles, and obliteration of the rectoprostatic angle (24). The features of seminal vesicle invasion at endorectal MR imaging include focal low signal intensity within and along the seminal vesicle (Fig 8), an enlarged low-signal-intensity seminal vesicle, enlarged low-signal-intensity ejaculatory ducts, obliteration of the angle between the prostate and the seminal vesicle, and demonstration of direct tumor extension from the base of the prostate into and around the seminal vesicle (Fig 8) (23).

MR imaging has been reported to have a wide range of sensitivities (13%–95%) and specificities (49%–97%) for detection of extracapsular extension, with a similarly wide range of sensitivities

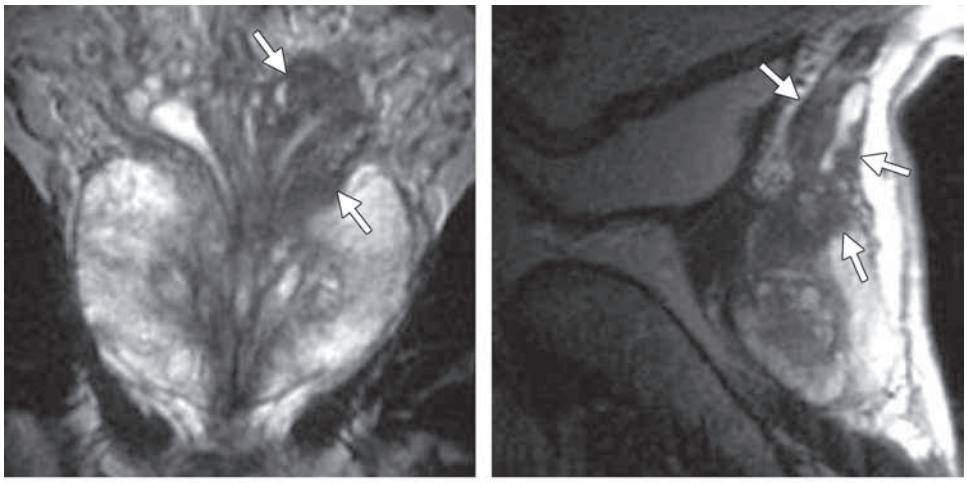

a. b.

**Figure 8.** Prostate cancer in a 64-year-old man with a prostatectomy Gleason score of 4 + 3 (tertiary pattern 5) (the presurgical biopsy score from a single fragmented 30% core was 3 + 3) and a PSA level of 3.4 ng/mL. The final histopathologic analysis showed a dominant nodule in the left posterolateral prostate at the base and midgland, with substantial extraprostatic tumor extension and seminal vesicle invasion at the left base. Endorectal MR imaging was performed at 1.5 T. **(a)** Coronal T2-weighted image (5000/93) shows concentric wall thickening of the left seminal vesicle (arrows) and dark tumor extending along the left seminal vesicle, findings compatible with seminal vesicle invasion. **(b)** Sagittal T2-weighted image (2900/92) shows continuity of the dark tumor, which extends from the left base into the left seminal vesicle (arrows).

(23%–80%) and specificities (81%–99%) for detection of seminal vesicle invasion (23,25). Limitations of conventional morphologic MR imaging of the prostate highlight the need for a combined anatomic and functional imaging approach.

## Diffusion-weighted Imaging and ADC Mapping

Diffusion-weighted imaging can add valuable information about tissue at the cellular level to the information from conventional T1-weighted and T2-weighted imaging (26). Because diffusion-weighted imaging measures the Brownian motion of water molecules, it provides important information about the functional environment of water in tissue and reflects the cellular status of normal and pathologic tissue.

Furthermore, diffusion-weighted imaging is sensitive to changes in the microdiffusion of water within the intracellular space and extracellular space and cytotoxic edema due to alterations in the adenosine triphosphate–dependent sodium-potassium pumps. Reduced diffusion of water in prostate cancer has been attributed to the increased cellularity of malignant lesions, with reduction of the extracellular space and restriction of the motion of a larger portion of water molecules to the intracellular space. Therefore, diffusion-weighted imaging provides an important quantitative biophysical parameter that can be used to differentiate benign from malignant prostate tissue (27).

Teaching Point

The amount of diffusion in tissue is determined by the diffusion coefficient *D*, which usually varies on subvoxel scales. The MR imaging–measurable spatially averaged biomarker of diffusion-weighted imaging is the ADC. The ADC quantifies the combined effects of both diffusion and capillary perfusion. A decreased ADC is interpreted as reduced motion of water molecules or diffusion, whereas in tissue with an increased ADC there is less restriction of water molecule motion.

The ADC has been related to the state of tissue during the growth of tumors or progression of cancer. With proliferating cells, there is an increase in cellular density and a decrease in the amount of intracellular space or extracellular space available, leading to a reduction in the ADC (Fig 4). Thus, diffusion-weighted imaging and ADC have become powerful indicators for characterization of prostate tissue, particularly in differentiation between benign and malignant lesions (27).

In general, regional ADC map values differ depending on location and tissue composition. Malignant lesions have lower ADC values (about

20%–40%) than benign or normal prostatic tissue. Also, there are regional variations in the normal tissue values for different zones of the prostate. Although in theory the ADC represents tissue properties only, in practice ADC measurements depend on the details of imaging unit hardware and imaging protocols. Therefore, comparison necessitates knowledge of the normal ranges for a specific system.

Some authors have stratified ADC values into benign and malignant and demonstrated that diffusion-weighted imaging and ADC mapping can increase the sensitivity (54%–98%) and specificity (58%–100%) of MR imaging in detection of prostate cancer when diffusion-weighted imaging is used in conjunction with T2-weighted imaging (28). Preliminary results suggest that diffusion-weighted imaging has the potential to increase the specificity of prostate cancer detection and to support prediction of tumor aggressiveness (29).

Acquisition parameters for diffusion-weighted imaging should be optimized according to the imaging unit and magnetic field strength used. The acquisition of different *b* values allows creation of matrix trace ADC maps on a pixel-by-pixel basis for quantitative analysis according to the following equation (30):

$$\mathrm{ADC} = \frac{-1}{n}\sum_{i=1}^{n}\frac{\ln\,(S_i / S_0)}{b_i},$$

where $b_i$ = the diffusion gradient values, $S_0$ = first image ($b = 0$), and $S_i$ = *i*'th image.

$$b = \gamma^2 G^2 \delta^2 (\Delta - \delta/3),$$

where $\gamma$ = gyromagnetic ratio, $G$ = gradient strength, $\delta$ = diffusion gradient duration, and $\Delta$ = time between diffusion gradient pulses.

The *b* value specifies the sensitivity of diffusion. Correctly assigning the *b* value for diffusion-weighted imaging is critical because it directly affects the ability to detect water molecule diffusion. As the *b* value increases, the amount of diffusion weighting increases and the sensitivity to diffusion increases. At high *b* value, diffusion-weighted imaging represents the molecular diffusion of water almost exclusively. However, as the *b* value increases, the gradient radiofrequency pulse is prolonged, thus increasing the echo time and reducing the quality of the diffusion-weighted images and the signal-to-noise ratio (SNR).

The smaller the *b* value, the higher the quality and SNR of the diffusion-weighted images; however, at the same time the T2 shine-through effect and tissue perfusion effects increase their influence on diffusion-weighted imaging. With lower *b* values, the ADC value also reflects the perfusion of the microcirculation, while the ability to reflect water molecule diffusion is worse than at higher *b* values (31). Traditionally, a set of images with a *b* value of 0 and another set with a *b* value of up to 1000 sec/mm$^2$ are acquired. The diffusion sensitivity can be varied to control the image contrast.

The approach to clinical interpretation of diffusion-weighted images in the diagnosis of prostate cancer must take into account several limitations of the technique, as outlined in the remainder of this section. In general, these limitations result in better performance in peripheral zone prostate cancer than in transition zone prostate cancer.

It has been reported that postbiopsy hemorrhage lowers the ADC of benign peripheral zone tissue and therefore limits the usefulness of diffusion-weighted imaging in this setting (31). However, more recent data demonstrated excellent ability of the ADC in differentiation of prostate cancer from hemorrhage in the peripheral zone, and it was suggested that delayed imaging after biopsy may not be necessary (32).

The location of prostate cancer affects the sensitivity of diffusion-weighted imaging. Noncancerous peripheral zone tissue has been found to have higher average ADC (less overlap with cancerous tissue) than the transition zone and prostate base. Overlap limits the ability to differentiate prostate cancer from noncancerous tissue (33). The high prevalence of BPH in elderly men significantly contributes to this difficulty. The stromal form of BPH in particular exhibits lower ADC and low T2 signal intensity, mimicking prostate cancer, whereas glandular BPH and prostatic intraepithelial neoplasia can be more readily distinguished because of their higher average ADC and higher T2 signal intensity (34).

Higher Gleason score has repeatedly been shown to be associated with decreased ADC, likely due to the dedifferentiated infiltrative growth of these tumors, as opposed to the glandular organization of more well-differentiated prostate cancer, which more closely resembles normal prostatic tissue (31,32).

Studies have found that ADC values in the central gland increase with age, in association

with the development of BPH (31). Therefore, diagnosis of prostate cancer with ADC measurements, especially in the central gland, may be less sensitive in younger patients.

Recently, high *b*-value diffusion-weighted imaging has been reported to increase diagnostic performance, sensitivity, and specificity in detection of prostate cancer (35), although other reports did not find significant increases in these parameters (36). The signal of diffusion-weighted imaging is dominated by the fast component of diffusion at standard *b* values; however, at least biexponential modeling is suggested for high *b*-value situations to take into account the slow diffusion component. Otherwise, deviation from the expected decrease in ADC with higher *b* values may result (36). High *b*-value imaging is hampered by further loss of the available signal owing to increased spin dephasing resulting from proton diffusion. To avoid prohibitive SNR loss, 3-T and endorectal coil techniques are favorable to compensate for these effects.

The advantages of diffusion-weighted imaging are short acquisition time and high contrast resolution between tumors and normal tissues. The shortcomings of diffusion-weighted imaging include susceptibility-induced distortions. These distortions are caused by susceptibility effects from the air-filled rectum or endorectal coil balloon, bone-tissue interfaces, poor local magnetic field homogeneity, and chemical shift artifacts caused by periprostatic fat. The susceptibility effects can be minimized by using rigid endorectal coils with no balloon or by filling the balloon with liquid perfluorocarbon or barium suspension.

## MR Spectroscopy

MR spectroscopy is also known as chemical shift imaging. The chemical shift is the physical phenomenon in which the electron cloud surrounding the imaged nucleus (in prostate MR spectroscopy, hydrogen nuclei = protons) shields the nucleus partially from the external field. Therefore, the nucleus exhibits a slightly different Larmor frequency. With $\omega_0$ being the Larmor frequency, $\gamma$ being the gyromagnetic ratio, and $B_0$ being the static magnetic field, the Larmor equation can be rewritten as follows:

$$\omega_0 = -\gamma B_0(1-\sigma),$$

where $\sigma$, the chemical shift, quantifies this electronic shielding and is highly dependent on the chemical environment (chemical bond, adjacent molecules or atoms) and the molecule the proton is located in.

Highly specific fingerprints of chemical compounds are the result in the form of MR spectra, which are made even more distinct by additional phenomena such as J coupling or chemical exchange (which are beyond the scope of this article). Some chemical compounds have simple spectra (a singlet or single spectral peak) while others possess highly coupled spectra with multiple spectral main peaks, each of which may be composed of multiplets (doublet, triplet, etc).

Little of this intricate physicochemical interplay can in fact be discerned with in vivo human MR spectra. This is because the effects of low SNR (due to use of lower field strength than achievable in tissue extracts and cell cultures), motion (arterial pulsations and bowel, bladder, or patient motion), imaging at the relatively high body temperature, and the need for localization of the MR spectroscopic signal to the prostate lead to spectral line broadening, which blurs many peaks into each other so that only compound peaks can be measured.

As can be seen from the preceding formula, the chemical shift $\sigma$ is a constant fraction of the reference Larmor frequency. Chemical shift is usually expressed in parts per million, a unit that means millionth parts of the reference Larmor frequency (commonly that of water). For example, at 1.5 T water protons precess at a Larmor frequency of approximately 64 MHz. Choline, with a chemical shift of 3.2 ppm, is therefore shifted by 3.2 ppm × 64 MHz = 205 Hz from the null point.

The null point is defined in MR spectroscopy as the MR resonance of tetramethylsilane in heavy water. It is known that by this standard, water resonates at 4.7 ppm; therefore, in vivo experiments are commonly calibrated to the water peak, with the scale set to 4.7 at the water resonance. Because MR spectroscopy provides important information about the biochemical and metabolic environment of the tissue, it is increasingly being used as a biomarker for detection of cancers, including prostate cancer (37).

Normal in vivo prostate spectra at different field strengths are shown in Figure 9. Citrate is found in fairly high concentrations (>60 mM) in healthy prostate epithelium and prostatic fluid; it is found in low concentrations elsewhere in tissue (38). The normal prostate has an MR spectrum with a prominent citrate peak at 2.6 ppm, which is usually seen as a doublet with occasional

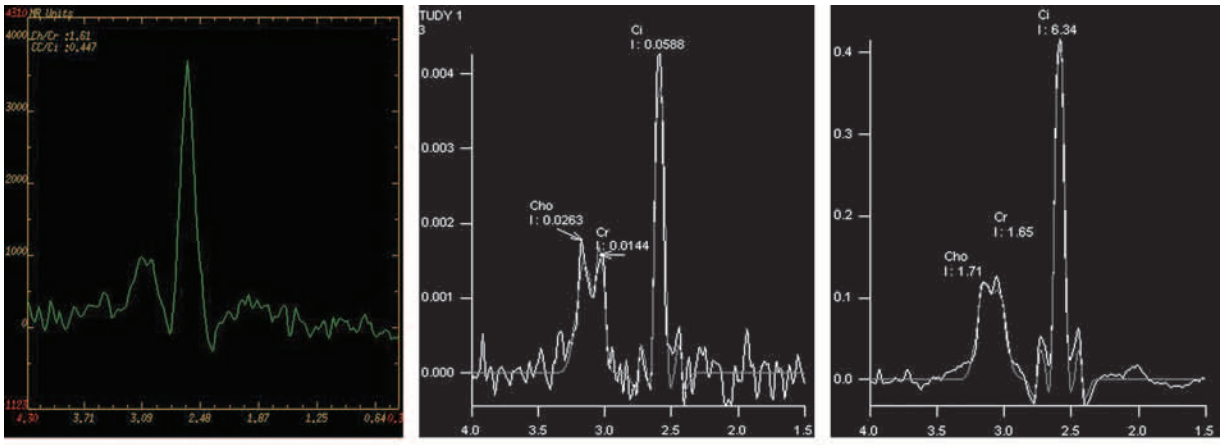


**Figure 9.** Comparison of MR spectroscopic spectra obtained in the peripheral zone of the normal prostate in different patients. **(a)** MR spectroscopic spectrum, obtained at 1.5 T with an endorectal coil, shows a high citrate *(Ci)* peak (resonance at 2.6 ppm) and a low choline *(Ch)* peak (resonance at 3.2 ppm), characteristics of benign tissue. The choline and creatine *(Cr)* peaks are overlapping. Ch + Cr/Ci = 0.447. **(b)** MR spectroscopic spectrum, obtained at 3 T with a body matrix coil, shows good separation of the choline *(Cho)* and creatine *(Cr)* peaks at higher magnetic field strength. The spectrum is normal, with a high concentration of citrate *(Ci)* and low concentration of choline. A diagnostic high-quality spectrum could be obtained with a noninvasive MR procedure without use of an endorectal coil. **(c)** MR spectroscopic spectrum, obtained at 3 T with an endorectal coil, shows a normal spectrum with a high citrate *(Ci)* peak and low choline *(Cho)* peak. Note the excellent spectral resolution of the citrate, choline, and creatine *(Cr)* metabolites, with only minimal baseline noise and detailed morphology of the citrate peak, which shows the effect of increased spectral resolution at 3 T, leading to a dominant central peak at 2.6 ppm with symmetric side peaks.

visualization of small additional side peaks. A decreased citrate level is found in prostate cancer, as well as in prostatitis and hemorrhage.

Choline is represented by its distinct methyl proton resonance, which forms a composite peak of phospholipid cell membrane components (eg, phosphocholine, glycerophosphocholine, and free choline) at 3.2 ppm. Owing to increased cell membrane turnover (phospholipid synthesis and degradation) and increased cell surface compared with cell volume in cellular tumors, choline concentrations are increased in prostate cancer. Increased choline signal or concentration is considered the spectroscopic hallmark of cancer (39); however, it has also been found in benign conditions of the prostate such as prostatitis (40).

Creatine resonates at 3.0 ppm and is related to energy metabolism. Normal prostatic tissue contains high polyamine levels, of which spermine is a predominant component. Polyamines are represented by a relatively broad spectral beak between creatine and choline (3.1 ppm) that shows significant overlap with creatine and choline. Polyamine levels are reduced in prostate cancer.

Lipids cause signal in a broad range at the lower end of the citrate peak (typically 1.3 ppm). Adequate placement of saturation bands around the prostate is important to avoid contamination of the spectra by inclusion of extraprostatic fat, which causes large lipid signals.

MR spectroscopy of the prostate requires use of multivoxel volume selection techniques. The most commonly used MR spectroscopic method is the point-resolved spectroscopy sequence (PRESS) (41). When applied to prostate imaging, PRESS provides increased SNR in comparison with that of alternative localization techniques, such as the stimulated-echo acquisition method (STEAM). After localization, single-voxel spectra can be obtained. However, more commonly, the PRESS volume is further subsectioned by using two- or three-dimensional phase-encoding gradients to perform MR spectroscopic imaging. In this fashion, a grid of multiple spectroscopic voxels can be collected at the same time, allowing coverage of the entire prostate.

In summary, the classic spectral signature of prostate cancer consists of increased choline and decreased citrate (Figs 5, 6). Because the spectra do not provide absolute metabolite concentrations in a straightforward fashion and calibration is complex, common approaches to MR spectroscopy take advantage of metabolite ratios, which allow comparison of changes in the relative quantities of metabolites present. Because citrate and choline vary in opposite directions in prostate

cancer, formulation of a ratio between them accentuates the change. An increase in the choline-to-citrate ratio or the (choline + creatine)/citrate ratio is often used as a marker of malignancy in prostate cancer and increases the specificity of diagnosis; however, it is most reliable in the peripheral zone.

Definition of spectra suspicious for prostate cancer can be performed in various ways, all of which set the measured spectral metabolites in relation to normal values. For example, a commonly used five-point MR spectroscopic scale scheme has been established (42). This scale is based on the known mean normal (choline + creatine)/citrate ratio, which is commonly given as 0.22 ± 0.013 (mean ± standard deviation [SD]) at 1.5 T (42). A score of 1 is assigned to ratios less than 1 SD above the mean. Subsequent scores are based on similar constructs (a score of 2 is <2 SDs above the mean, a score of 3 is <3 SDs above the mean, a score of 4 is <4 SDs above the mean, and a score of 5 is ≥4 SDs above the mean). Scores of 3 or more are commonly interpreted as suspicious, with individual scores interpreted as equivocal for cancer (score of 3), probably malignant (score of 4), and likely malignant (score of 5) (Fig 6).

Although MR spectroscopy shows promise as a problem-solving modality with high specificity, it is limited by low sensitivity. Partial volume effects may obscure the presence of prostate cancer, especially small or infiltrative lesions, which are obscured by strong signals from glandular BPH or surrounding normal tissue present in the MR spectroscopic voxels. By shifting the MR spectroscopic voxels to a position centered on the area of suspected abnormality, a voxel containing the highest possible partition of abnormal tissue can be generated; with this method, some of the lost information can occasionally be recovered. The extracellular lakes of mucin in the rare (0.4% of all prostate adenocarcinomas) and aggressive mucinous subtype of prostate cancer often make this cancer undetectable at both T2-weighted imaging and MR spectroscopy (43).

Despite the relatively high specificity of MR spectroscopy, false-positive MR spectroscopic interpretations can result from inclusion of signal from the seminal vesicles, stromal BPH, prostatitis, and focal prostatic atrophy (44). Although the (choline + creatine)/citrate ratio can be low or normal in BPH (Fig 3), this is the case predominantly in glandular BPH, which has high levels of citrate and polyamines as a result of the histologic composition of hyperplastic glandular tissue. In stromal BPH, however, citrate and polyamine levels can be strongly suppressed and there may be elevation of choline due to the presence of proliferative elements, leading to significant overlap with the findings of prostate cancer. In addition, prostatitis has previously been found to be able to mimic prostate cancer (45). This leads to possible significant difficulty in distinguishing prostate cancer from prostatitis and stromal BPH, especially in the transition zone.

When combined with anatomic imaging, MR spectroscopy has been found to increase the accuracy of tumor volume estimation in prostate cancer (46), although other data have shown lack of an additional advantage. More recent data have shown significantly increased choline-to-citrate ratios and larger tumor volumes in stage T2b or higher tumors than in stage T2a or lower tumors, further suggesting a potential of MR spectroscopy for tumor volume estimation and staging (47). However, currently data are too sparse to determine if MR spectroscopy can surpass other modalities for this purpose.

Multiple MR spectroscopy software packages are commercially available, allowing performance of routine clinical prostate MR imaging. Several challenges remain in the clinical application of MR spectroscopy. Complex postprocessing of the prostatic spectra requires significant operator skill to achieve reproducible data. To achieve high-quality data, adequate saturation band placement is needed to suppress signals from periprostatic tissues. Optimal shimming must be performed to achieve optimal magnetic field homogeneity over the MR spectroscopic volume, a process that can be time-consuming.

Susceptibility effects from endorectal balloon air, air in the rectum, or motion artifacts may decrease spectral quality and limit the ability to acquire high-quality data. The lower resolution of MR spectroscopy demands minimization of diagnostically decisive partial volume effects. A significant number of spectral voxels acquired may contain nondiagnostic levels of metabolites owing to poor SNR related to suboptimal shimming and motion artifacts. Postbiopsy hemorrhage is known to degrade MR spectra (48). However, it was shown that MR spectroscopy may improve diagnostic accuracy for cancer in the presence of postbiopsy hemorrhage, when findings on T2-weighted images are nondiagnostic (49).

## Dynamic Contrast-enhanced MR Imaging

DCE MR imaging is an advanced prostate imaging modality that allows derivation of parameters that are closely related to microvascular properties and angiogenesis in tissues. Tumor hypoxia and the expression of angiogenesis-inducing factors, such as vascular endothelial growth factor, induce budding of new blood vessels from existing blood vessels (angiogenesis) or de novo formation of blood vessels (vasculogenesis). Tumor neovessels are in general more permeable than normal vessels, more heterogeneous in size and branching pattern, and disorganized.

Teaching Point

In prostate cancer, increased tumor vascularity leads to early hyperenhancement (higher and earlier peak enhancement than in normal tissue) and to rapid washout of contrast material from the tumor, in comparison with normal prostate tissue (Fig 4). Microvascular alterations and neovascularity are in general most severe in prostate cancer, in comparison with other processes in the prostate such as BPH or prostatic intraepithelial neoplasia (50). DCE MR imaging uses a pharmacokinetic tracer kinetic compartmental model (TKCM) to describe the microscopic processes leading to the distribution of molecules of contrast agent (most commonly a gadolinium chelate, which is referred to as *the tracer*) between the vascular and extravascular spaces over time.

The TKCM is mathematically complex, and the reader is referred to the literature for more detail (25,51). Different TKCMs can be employed, which vary in their complexity. The more compartments are included to model the intravoxel signal behavior, the more data are needed to achieve reasonable convergence of the model parameters.

Classically, a four-compartment Tofts model (52) is used, which models the intravoxel signal by using a intravascular blood plasma compartment and an extracellular-extravascular space (EES) compartment. It also includes the whole-body vascular and extracellular space and a kidney excretory pathway to model the behavior of contrast agent dilution, recirculation, and excretion. In kinetic modeling, the transfer constant $K^{trans}$, which describes microvascular permeability and blood flow, and the EES volume fraction or leakage space $v_e$ in the tissue represent the two main differentiating parameters of cancer. These parameters are derived as follows:

The known variables in the TKCM are the time variation of the tracer concentration in the artery supplying the tissue of interest (the input artery) and the tissue tracer concentration (Fig 10). In fact, only the signal intensity change between the unenhanced and enhanced phases is known, and assumptions are made to convert this signal intensity change into absolute concentrations. Input artery and tissue tracer concentrations are zero at the beginning of the examination. After intravenous injection of the tracer, the tracer concentration first rises in the input artery and subsequently the tissue is observed to enhance, meaning that the signal intensity in the tissue voxels is caused to change by the presence of the tracer.

Ideally, one measures the input artery concentration as close to the tissue of interest as possible. In practice, this is limited by the identification of a large enough artery from which to derive a reliable ROI for assessment of tracer concentration. Commonly, the external iliac artery is chosen. The concentration-time course observed in the input artery is called the arterial input function. Although the input arterial lumen is large in comparison with the voxel size, the processes underlying the observed tissue enhancement are below the resolution of MR imaging.

In a small MR imaging voxel, tissue arterioles, venules, capillaries, and neovessels follow the blood pool tracer concentration, in that their contrast agent concentration is similar to the arterial input function, although it is delayed by the time it takes the bolus to travel from the input artery ROI to the tissue voxel and altered by hematocrit changes in the microvasculature. The tracer does not stay intravascular only, because the vascular endothelium and the microvascular boundaries allow the tracer to diffuse into the EES according to the concentration gradient between the intravascular space and the EES. Once the vascular contrast agent bolus has passed the capillaries, the tissue concentration will be higher in the EES, and back-diffusion of the tracer into the intravascular space will occur, leading to washout of contrast agent from the tissue.

Therefore, tissue enhancement provides information about the microvascular properties, the extravascular space, and the exchange rate between these compartments. Enhancement will be strong and fast if many tumor vessels exist, occupying a relatively large fraction of the voxel. Enhancement will also be strong and reasonably fast if the surface area of the microvessels is large and their walls are highly permeable, allowing fast exchange between the intravascular space and EES. In both cases, washout from the tissue will be fast for the same reasons.

TKCM is a concept well known from the fields of pharmacology and nuclear medicine, where many of the mathematical foundations were first derived. The unknown parameters in the TKCM

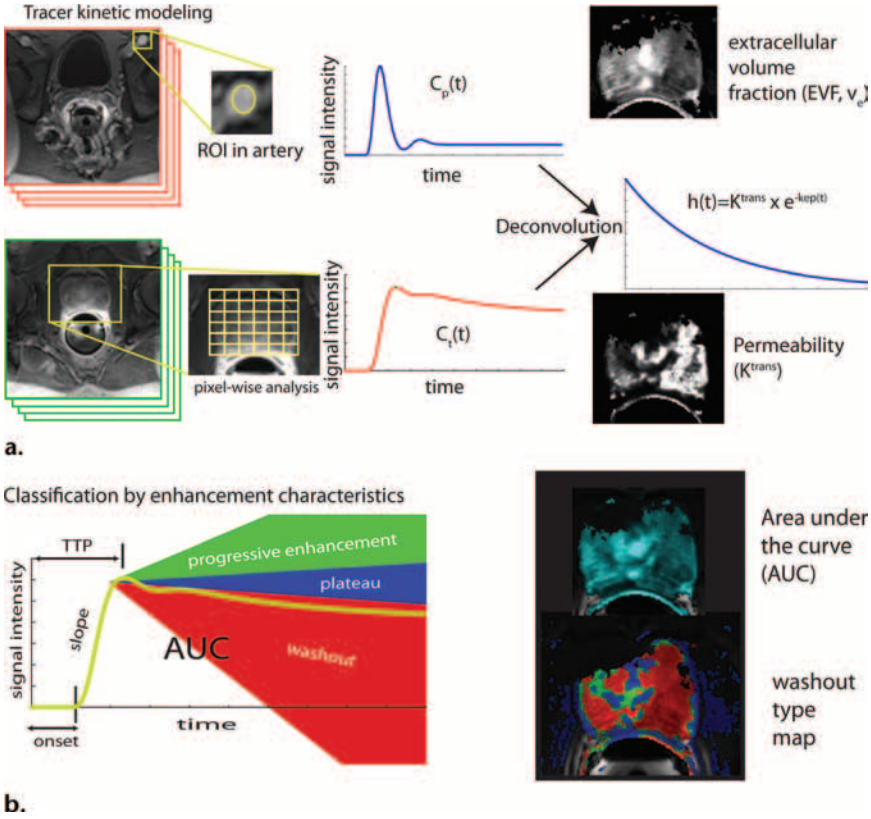


**Figure 10.** Synopsis of DCE MR imaging. **(a)** Use of the TKCM. Repeated imaging before and after administration of contrast material is performed. ROI analysis of the input artery (top) and voxel-wise analysis of the prostate (bottom) yield the arterial input function and voxel-wise time-concentration curves. Mathematical deconvolution is used to recover the tissue response *h(t)*, from which the TKCM parameters can be estimated. Parametric maps are generated by color-coding ranges of TKCM parameters according to nomograms. *kep* = efflux rate constant, $K^{trans}$ = influx transfer constant, $v_e$ = leakage space. **(b)** Heuristic parameters are illustrated for a tissue time–signal intensity curve. These include onset time, slope, time to peak *(TTP)*, washout characteristics (progressive enhancement, plateau, and washout), and area under the curve *(AUC)*. Parametric maps are pseudocolored to facilitate recognition of suspicious parameter values.

are commonly called the leakage space ($v_e$), efflux rate constant ($k_{ep}$), and influx transfer constant ($K^{trans}$). These parameters are connected by the following equation: $v_e = K^{trans}/k_{ep}$. The leakage space is the EES volume fraction, which is the percentage of volume in the MR imaging voxel that is occupied by the EES. $K^{trans}$ determines the flux from the intravascular space into the EES; it may represent the blood flow into the tissue in a flow-limited situation (high permeability relative to flow), or it may predominantly represent the vascular permeability in a permeability-limited situation (high flow relative to permeability) (51).

It is important to be aware that $K^{trans}$ does not directly represent permeability or blood flow alone. However, in many tumors, flow and permeability are higher than in normal tissue and therefore $K^{trans}$ will be elevated, due to a mixed effect of increased flow and permeability. It is an advantage that the parameters influencing $K^{trans}$—permeability, microvascular surface area, microvascular fractional volume, and microvascular blood flow—are commonly altered in concert in such a way that $K^{trans}$ is synergistically elevated in tumor neoangioneogenesis. This may explain why $K^{trans}$ has been identified as one of the most useful parameters in DCE MR imaging to date.

The EES fractional volume ($v_e$) commonly decreases in tumors when the neovessels occupy a higher fraction of the voxel volume than in normal tissue. However, a $v_e$ decrease has been found to be less specific for prostate cancer than is $K^{trans}$. $v_e$ can be similar in BPH, the normal transition zone, and prostate cancer (53,54).

The TKCM has an enormous and currently largely unused potential in its application to DCE MR imaging. In fact, the most established parameters in DCE MR imaging are not based on the TKCM but are heuristic parameters, which are descriptive and empirically derived and do not directly represent an underlying pathophysiologic correlate, as opposed to the TKCM parameters, which reflect microvascular properties. Heuristic parameters are also known as time–signal intensity parameters, as they describe the important features of the tissue enhancement curve. These include the onset time, mean gradient, time to peak enhancement, magnitude of peak enhancement, and washout characteristics (Fig 10).

The onset time is defined as the time delay between the onset of bolus injection of the tracer and the time point of signal intensity increase above 10% of the peak enhancement. The mean gradient is the average rate of change of the relative signal intensity between the points of 10% and 90% peak enhancement. Maximum signal intensity or peak enhancement is defined as the highest signal intensity during the dynamic acquisition period. Washout characteristics are usually grouped into the three observations of washout, plateau enhancement, and progressive enhancement. They are dependent on whether there is significant signal intensity decrease after peak enhancement, no significant change, or no maximum reached during the first minutes, respectively.

To some degree, heuristic parameters can be related to TKCM parameters. The rate of enhancement is thought to be reflective of the vascular volume and the permeability of the vessels, while the magnitude of enhancement likely reflects the extravascular-extracellular leakage space (55).

In prostate cancer, there is early, rapid, and intense enhancement with quick washout of contrast material (Fig 4). The presence of washout is highly indicative of prostate cancer (56), even in the absence of low T2 signal intensity (Fig 5). In prostate cancer, onset time and time to peak enhancement are lower and peak enhancement is higher than in high-grade prostatic intraepithelial neoplasia and chronic inflammation, and abnormalities are more distinct in high-grade prostate cancer (57). All DCE MR imaging parameters can be converted into pseudocolor parametric maps and overlaid on the anatomic T1- and T2-weighted images for interpretation (Figs 3–6).

Criteria for extracapsular extension or seminal vesicle invasion at DCE MR imaging include abnormally high or asymmetric peak enhancement, contrast agent washout, and short onset time and time to peak enhancement. In the case of extracapsular extension, these findings are detected near the neurovascular bundle or rectoprostatic angle, broadly abutting the capsule, or in an extracapsular location. In seminal vesicle invasion, these abnormalities are found in the lumen of the ejaculatory ducts or in the seminal vesicles themselves and are associated with wall thickening of the ejaculatory ducts.

DCE MR imaging can improve the staging accuracy of less-experienced readers for detection of capsular penetration and seminal vesicle invasion and can allow detection of cancers that are not apparent on T2-weighted images. In addition, in multifocal cancers, DCE MR imaging may demonstrate additional foci of higher stage than the known lesions, leading to adequate upstaging of tumors (58).

DCE MR imaging forms part of the current advanced multiparametric MR imaging approach for evaluation of prostate cancer. DCE MR imaging in combination with MR spectroscopy allows detection of prostate cancer in 46% of patients with prior negative transrectal US–guided biopsy results and a persistently elevated PSA level (4–10 ng/mL), versus a prostate cancer detection rate of 24% with repeat transrectal US–guided biopsy in these patients (59). A parametric model using the diffusion-weighted imaging parameter ADC, results of quantitative T2-weighted imaging, and $K^{trans}$ was found to have the best performance in a logistic regression analysis (53).

Although much progress has been made, challenges for DCE MR imaging remain. Current DCE MR imaging techniques may not allow differentiation of prostatitis from cancer in the peripheral zone or distinction between BPH and transition zone tumors, but differences in the initial enhancement amplitude and washout patterns have been reported (50). Figure 6 depicts a case of transition zone prostate cancer, whereas Figure 3 shows findings in BPH; the comparison illustrates use of histogram analysis of $K^{trans}$ for the differentiation.

Prostatic intraepithelial neoplasia and well-differentiated prostate cancer demonstrate less neovascularity and permeability changes than does higher-grade prostate cancer and therefore represent a source of false-negative results at DCE MR imaging. Differentiation of chronic prostatitis from low-grade prostate cancer may not be possible, while differences were found in DCE MR imaging parameters between high-grade prostate cancer and chronic prostatitis (60). In addition, low tumor volumes and infiltrative prostate cancer are affected by partial volume effects and are more difficult to detect.

Although heuristic parameters are generally quite useful clinically and generally show good agreement with TKCM parameters, they are limited by their qualitative or semiquantitative nature. The advantage of TKCM parameters is their direct relationship to pathophysiologic properties of the examined tissue. In practice, this advantage is limited by dependence on accurate estimation of the arterial input function and sequence parameters; however, use of TKCM parameters is superior in the settings of interindividual quantitative comparisons and posttherapy follow-up. BPH may demonstrate washout characteristics suggestive of malignancy, and histogram analysis of TKCM parameters may be helpful in differentiation from prostate cancer (Figs 3, 6).

## Prostate MR Imaging at 3 T versus 1.5 T

Prostate MR imaging at 1.5 T has been well established, and use of an endorectal coil with a 1.5-T MR imaging system is considered indispensable for diagnostic quality imaging. With the growing availability of 3-T whole-body MR imaging units, new opportunities arise for clinical and research applications in prostate imaging.

The fundamental impetus for the migration to higher static magnetic field strengths lies in an increased SNR (which increases linearly with the static magnetic field $B_0$) and increased spectral resolution. The SNR gain at 3 T can be used in multiple ways. In comparison with 1.5-T imaging, improvements in spatial or temporal resolution and in patient comfort—when no endorectal coil is used—are possible. At 3 T, the spatial resolution can reach 0.18 mm with use of an endorectal coil, while it is near 0.55 mm at 1.5 T. Imaging voxel sizes can be reduced to 0.13 $mm^2$ at 3 T, while the smallest voxel sizes are about 1.21 $mm^2$ at 1.5 T (61). Both conventional T1- and T2-weighted imaging techniques and the new multiparametric MR imaging protocols benefit significantly from imaging at higher field strength, when the potential sources of increased image distortion or signal loss and the specific challenges of higher-field-strength imaging are considered.

In comparison with 1.5-T imaging, the power deposition by radiofrequency pulses increases fourfold, if the same imaging sequences are used. Prostate imaging benefits from lower specific absorption rate sequences, many of which have been developed initially for 3-T applications in other body regions. Power deposition can be reduced by using a lower number of phase-encoding steps with parallel imaging techniques, increased repetition time or decreased flip angle, or modified radiofrequency pulses, which may be of longer duration. Shorter T2 and longer T1 relaxation times at 3 T, increased susceptibility and dielectric effects, and signal heterogeneity from larger magnetic field variations can be addressed by using thinner sections, higher spatial resolution, or higher bandwidth. Radiofrequency penetration effects can compromise radiofrequency field homogeneity. Most of these compensatory techniques imply an inherent SNR reduction, which has to be controlled and optimized in 3-T–specific imaging protocols.

Imaging without endorectal coils is feasible at 3 T and helps decrease patients' reluctance to undergo an uncomfortable and invasive examination, while allowing simpler patient preparation for the study. Although essential at 1.5 T, use of endorectal coils is itself accompanied by technical challenges, which reach beyond the patient comfort factors. The inhomogeneous endorectal coil receive field has its highest sensitivity directly adjacent to the coil surface and spans a relatively small area, mandating optimal anatomic positioning to take most advantage of the addition of the coil. At 3 T, image quality comparable with that at 1.5 T can be achieved without use of endorectal coils (62). However, if endorectal coils are used, significant improvements in localization and staging of prostate cancer have been reported in comparison with use of phased-array surface coils only (63).

Endorectal coils are prone to introducing strong susceptibility gradients, especially if air is used to inflate the coil balloon. Although common practice at 1.5 T, use of air inflation at 3 T often causes prohibitive artifacts; therefore, balloon distention is often achieved by using substances that are more similar to the tissue susceptibility (eg, liquid perfluorocarbon or barium) (64). Rigid coils that avoid the need for inflatable balloons have been developed for use at 1.5 T and were found to provide approximately 2.5-fold higher SNR near the peripheral zone midline than did inflatable coils, while being devoid of the strong susceptibility gradients asociated with endorectal inflatable balloon coils.

The novel functional and physiologic MR imaging techniques (MR spectroscopy, diffusion-weighted imaging, and DCE imaging) specifically benefit from the migration to 3 T for prostate imaging, as discussed in the remainder of this section.

MR spectroscopy inherently benefits from higher field strengths as a result of the inability to increase the spectral resolution with other methods. Spectral line broadening is introduced by physiologic and thermal effects, and only

transition to higher field strengths will reduce the line width in relation to the constant chemical shift of the coupled and uncoupled metabolite protons of interest, thus making them better discernible (Fig 9). At 1.5 T, the spectral quality may prohibit routine separation of closely adjacent peaks such as the choline, polyamine, and creatine peaks, which are therefore often combined into a single parameter (eg, the [choline + creatine]/citrate ratio) for analysis.

In addition, the SNR gain benefits MR spectroscopy, which is a low-SNR technique, in that faster data acquisition and imaging at smaller voxel sizes (at higher resolution) become feasible. Voxel sizes for 3-T MR spectroscopy of 0.15 $cm^3$ can be achieved with use of an endorectal coil, while the voxel size for 1.5-T MR spectroscopy has been found to be limited near 0.30 $cm^3$ (65). Smaller voxel sizes are desirable to reduce volume averaging of tumors with periprostatic fat, the seminal vesicles, postbiopsy hemorrhage, or periurethral tissues. Both better spatial resolution and better spectral resolution improve the ability to detect and characterize tumors with MR spectroscopy.

Diffusion-weighted imaging is another low-SNR technique that benefits from higher field strengths, allowing higher-quality imaging and higher spatial resolution (66). Technical challenges at higher field strength include increased susceptibility artifacts and greater chemical shifts. However, use of parallel imaging (67) can reduce some of these artifacts by reducing the number of phase-encoding steps for a full acquisition, thus allowing adjustment of other parameters (echo spacing and echo train length), and by use of multiple shots during an echo-planar imaging readout. Diffusion-weighted imaging benefits from the concurrent use of endorectal coils with 3-T magnets, as the signal gain can be fully deployed for higher resolution or better image quality.

ADC measurements depend on both field strength and sequence parameters, so that results from 1.5-T and 3-T imaging systems may be different despite examination of the same underlying physiologic processes. Separation of tumor from healthy parenchyma is improved with 3-T diffusion-weighted imaging in comparison with 1.5-T diffusion-weighted imaging, and the ADC has been found to be significantly lower in prostate cancer than in normal tissue (68). Because the sensitivity of diffusion-weighted imaging to susceptibility artifacts and distortions is increased at 3 T, significant motion artifacts need to be avoided by limiting gross motion of the patient and suppressing rectal peristalsis (eg, by intravenous administration of glucagon before the examination).

Because DCE MR imaging is a demanding technique that requires high temporal resolution, high spatial resolution, and adequate volume coverage of the prostate at the same time, it is limited by the performance of imaging equipment at 1.5 T. In DCE MR imaging at 1.5 T, the temporal resolution is often a limiting factor to preserve spatial resolution. Increased spatial resolution reduces volume averaging and allows detection of smaller tumor foci and more precise tumor volume assessment. However, adequate temporal sampling is necessary for estimation of pharmacokinetic parameters with higher fidelity to reduce overlap between malignant and benign tissue.

Both spatial and temporal resolution must be sufficiently high at the same time to permit a useful DCE MR imaging protocol, and DCE MR imaging will best achieve its potential at higher field strengths such as 3 T. In an experimental animal model, it has been shown that decreased temporal resolution (15–85 seconds) leads to underestimation of the transfer constant $K^{trans}$ (4%–25%) and to overestimation of the fractional EES volume $v_e$ (1%–10%) (69). This underlines the importance of high-temporal-resolution imaging (preferably <10 seconds per phase). The temporal resolution increase relies on fast pulse sequences and benefits from the increased SNR at higher field strengths.

In summary, detection, localization, and staging of prostate cancer benefit from the higher achievable spatial resolution and increased SNR at 3 T, as tissue interfaces are better visualized and lower-contrast structures are better identified. Combination of functional techniques with anatomic imaging has been reevaluated at 3 T. Although DCE MR imaging and MR spectroscopy alone had lower sensitivity than T2-weighted imaging, combination of both had higher specificity (97%–99% for MR spectroscopy, 96%–97% for DCE MR imaging) than did T2-weighted imaging (83%–89%), and their addition increased the overall accuracy and predictive value of conventional T2-weighted imaging for accurate localization of prostate cancer (70).

In the experience of the authors, the concurrent use of endorectal coils allows one to take full advantage of the increased SNR for more detailed imaging of the prostate, and this approach is best able to answer new research and clinical questions. On the other hand, the ability to perform high-quality imaging without the use of endorectal coils is a significant factor that makes prostate MR imaging attractive to patients who would otherwise hesitate to undergo the examination, and this technique should be offered to such patients.

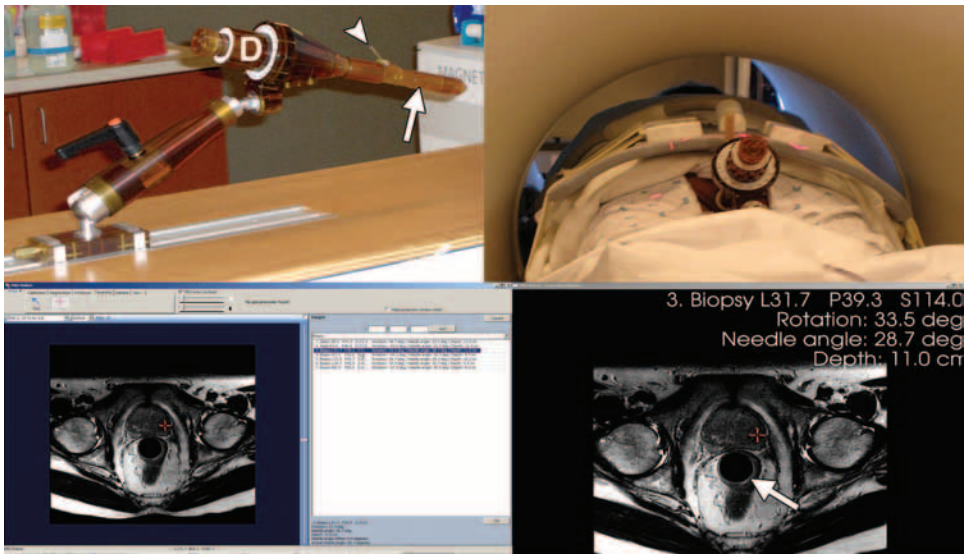


**Figure 11.** MR imaging–guided prostate biopsy. Photographs (top) and computer screens (bottom) show use of an MR imaging–compatible biopsy device (72). The device (top left) has an endorectal probe (arrow), a needle guide (arrowhead), and a set of dials *(D)*, which allow the needle to be directed to the target on the basis of input from the targeting software (bottom left). The software provides the necessary angles for probe rotation, needle angulation, and needle depth (bottom right). The dials are adjusted manually by the operator on the basis of software calculations derived from prebiopsy targeting MR images. The patient is placed in the prone position (top right) with endorectal placement of the biopsy probe (arrow at bottom right).

## MR Imaging–guided Biopsy

The limitations of transrectal US with biopsy were outlined earlier. New instruments for image-guided interventions are needed to increase the accuracy and repeatability with which needles are placed in the prostate. Because MR imaging provides more detailed anatomic images of the prostate than does transrectal US and because it has been shown to be the most accurate imaging modality for localization of prostate cancer, MR imaging–based guidance offers the possibility of more precise targeting, which may be crucial to the success of modern diagnostic and local therapeutic interventions in the prostate.

Real-time virtual sonography is a technique in which the MR imaging dataset is coregistered to landmarks during the US examination, so that a needle can be placed sonographically. However, experience with this technique is currently limited (71). The advantage of MR imaging–guided needle placement appears to be the temporal proximity of imaging and needle placement with the option of real-time visualization of the target, while the patient remains in the same position (Fig 11), thus reducing the effects of differing position and distention of pelvic structures (bladder, rectum, areas of peristalsis) on the location and shape of the prostate.

The usefulness of MR imaging–guided biopsy has been recognized. Transrectal MR imaging–guided prostate biopsies and brachytherapy have been performed in a closed-bore 1.5-T imaging unit (72). Preliminary evidence suggests that MR imaging–guided biopsy may improve cancer detection (73).

Providing guidance with MR imaging poses several challenges. Access within the MR imaging unit is limited for manual instrument handling, and development of new instrumentation for use in the MR imaging environment is demanding. MR imaging–compatible robots are being purposely designed to operate in the space and environmental restrictions inside the MR imaging unit, allowing real-time interventions. Material restrictions (nonferromagnetic components) apply, and actuators and sensors without electric currents are preferred.

Robotic prostate biopsy promises high accuracy and is a topic of intense research. Prototypes of MR imaging–compatible robots are being developed at several institutions (74). At the authors' institution, a fully automated MR imaging–compatible "stealth" robot has been developed (Fig 12) (75), which is currently designed for

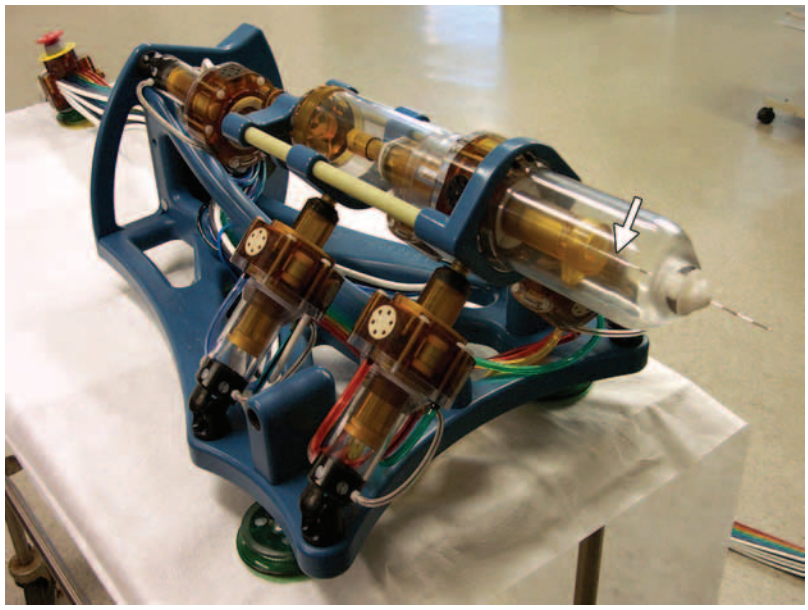

**Figure 12.** Photograph of an MR imaging–compatible stealth prostate intervention robotic device (currently an investigational device). Note the needle driver (arrow), which is automatically manipulated with a pneumatic motor. The device can operate in the gantry of an MR imaging unit alongside the patient in the decubitus position and can be actuated remotely.

transperineal needle access to the prostate. This robot can perform biopsies and automatically place brachytherapy seeds in the prostate. It possesses six degrees of freedom: five for positioning and orienting the injector and one for setting the depth of needle insertion. High accuracy of registration with targeting errors due to registration as low as 0.3 mm have been achieved. The robot was tested on a canine model and is currently being tested for human use.

As technology matures, precise image guidance for prostate interventions performed or assisted by specialized MR imaging–compatible robotic devices may provide a uniquely accurate solution for directly guiding the intervention on the basis of MR imaging findings and feedback. Such an instrument would become a valuable clinical tool for biopsies, directly targeting imaged tumor foci and delivering tumor-centered focal therapy. Further research is needed to define the indications for MR imaging–guided procedures (eg, persistently elevated PSA level in the setting of a prior transrectal US–guided prostate biopsy with negative results or identification of larger than expected tumor foci in patients undergoing active surveillance who may need curative intervention) and to define the patient populations who could benefit most from these procedures.

## Development of an Imaging Algorithm

After reviewing the complexity of multimodality prostate MR imaging, the question arises how to select the appropriate technique for an individual patient. The general trend in the existing literature is that addition of functional imaging to anatomic imaging increases the accuracy of prostate cancer assessment with MR imaging. In general, the more imaging modalities are combined, the better the accuracy seems to be. For example, recent data have shown that T2-weighted imaging, MR spectroscopy, and DCE MR imaging show synergy in reaching a high probability of tumor detection (70).

Given the variability in technical parameters, a prerequisite to take advantage of multimodality imaging is institutional optimization of each sequence to achieve optimal performance. This includes optimal shimming and saturation band placement for MR spectroscopy, standardized injection of contrast material and determination of arterial input function for DCE MR imaging, and standardized *b* value use for diffusion-weighted imaging. Quality control should be performed regularly to assure that all parts of the protocol are optimized. After these prerequisites are met, protocol adjustment can be performed according to the individual situation.

For example, in the presence of hemorrhage, data suggest that diffusion-weighted imaging should be included (32). Posthemorrhage detection of prostate cancer has been found to benefit from inclusion of MR spectroscopy and DCE MR imaging as well (49). Use of an endorectal coil and 3-T imaging should be preferred in general, with the option to offer 3-T imaging without use of an endorectal coil to attract patients who would otherwise elect not to undergo MR imaging. In

patients with contraindications to administration of gadolinium contrast agents, such as low glomerular filtration rate, DCE MR imaging will have to be avoided. In the setting of prior pelvic surgery, susceptibility artifacts from surgical slips or hardware may impede achievement of high-quality diffusion-weighted imaging and MR spectroscopy.

Assessment of transition zone cancer is thought to benefit more from use of diffusion-weighted imaging in patients of more advanced age (31). Differentiation of peripheral zone cancer from prostatitis and of BPH from transition zone cancer may benefit from use of DCE MR imaging with the TKCM. At the authors' institution, anatomic imaging, diffusion-weighted imaging, and DCE MR imaging are part of the standard MR imaging protocol for prostate cancer. MR spectroscopy is performed regularly; however, it requires dedicated protocol selection by the radiologist reviewing the order and is used when deemed appropriate for problem-solving purposes.

## Summary

Much advancement has recently been made in the evaluation of prostate cancer with MR imaging. The result is an integrated concept of multimodality imaging of the prostate, in which classic anatomic imaging with T1- and T2-weighted imaging is combined with novel functional techniques including diffusion-weighted imaging, DCE MR imaging, and MR spectroscopy. Significant improvements have been made in the accuracy of MR imaging in diagnosis, localization, and staging of prostate cancer. Owing to the morbidity associated with prostate cancer treatments, increased diagnostic and staging accuracy is of high importance for accurate treatment selection. In addition, existing MR imaging protocols have benefited from improvements in imaging unit hardware and postprocessing techniques, such as higher field strength, parallel imaging, faster imaging, and use of multiparametric maps.

Owing to its exquisite soft-tissue contrast, MR imaging is well suited for assessment of the prostate. New developments in robotics and interventional MR imaging techniques benefit from the advantages of MR imaging in guiding biopsies, enabling excellent adjustment and confirmation of needle position during the procedure. MR imaging is a rapidly evolving field, and the application of many new techniques to the evaluation of prostate cancer will continue to improve the diagnostic accuracy of prostate cancer assessment with MR imaging and is expected to continue to significantly improve patient care.

## References


1. American Cancer Society. Prostate cancer facts. In: Cancer facts & figures 2009. Atlanta, Ga: American Cancer Society, 2009; 19–20.
2. Slawin KM, Diblasio CJ, Kattan MW. Minimally invasive therapy for prostate cancer: use of nomograms to counsel patients about the choice and probable outcome of therapy. Rev Urol 2004;6 (suppl 4):S3–S8.
3. Thompson IM, Pauler DK, Goodman PJ, et al. Prevalence of prostate cancer among men with a prostate-specific antigen level < or =4.0 ng per milliliter. N Engl J Med 2004;350(22):2239–2246.
4. Okotie OT, Roehl KA, Han M, Loeb S, Gashti SN, Catalona WJ. Characteristics of prostate cancer detected by digital rectal examination only. Urology 2007;70(6):1117–1120.
5. Stamey TA, Freiha FS, McNeal JE, Redwine EA, Whittemore AS, Schmid HP. Localized prostate cancer: relationship of tumor volume to clinical significance for treatment of prostate cancer. Cancer 1993;71(3 suppl):933–938.
6. Pelzer AE, Tewari A, Bektic J, et al. Detection rates and biologic significance of prostate cancer with PSA less than 4.0 ng/mL: observation and clinical implications from Tyrol screening project. Urology 2005;66(5):1029–1033.
7. Basso D, Fogar P, Piva MG, et al. Total PSA, free PSA/total PSA ratio, and molecular PSA detection in prostate cancer: which is clinically effective and when? Urology 2000;55(5):710–715.
8. Spajic B, Eupic H, Tomas D, Stimac G, Kruslin B, Kraus O. The incidence of hyperechoic prostate cancer in transrectal ultrasound-guided biopsy specimens. Urology 2007;70(4):734–737.
9. Svetec D, McCabe K, Peretsman S, et al. Prostate rebiopsy is a poor surrogate of treatment efficacy in localized prostate cancer. J Urol 1998;159(5): 1606–1608.
10. Jemal A, Siegel R, Ward E, et al. Cancer statistics, 2008. CA Cancer J Clin 2008;58(2):71–96.
11. Patel AR, Jones JS, Rabets J, DeOreo G, Zippe CD. Parasagittal biopsies add minimal information in repeat saturation prostate biopsy. Urology 2004;63(1): 87–89.
12. Presti J Jr. Does the yield of prostate cancer biopsy and repeat biopsy justify the frequency of their use? Nat Clin Pract Urol 2008;5(5):246–247.
13. Webb JA, Shanmuganathan K, McLean A. Complications of ultrasound-guided transperineal prostate biopsy: a prospective study. Br J Urol 1993;72(5 Pt 2):775–777.
14. Dotan ZA. Bone imaging in prostate cancer. Nat Clin Pract Urol 2008;5(8):434–444.
15. Weidner A, Michaely HJ, Pelzer A, et al. Imaging of prostate cancer by diagnostic radiology and nuclear medicine. Aktuelle Urol 2010;41(1):35–42.
16. Lacy GL 2nd, Soderdahl DW, Hernandez J. Optimal cost-effective staging evaluations in prostate cancer. Curr Urol Rep 2007;8(3):190–196.
17. McNeal JE, Redwine EA, Freiha FS, Stamey TA. Zonal distribution of prostatic adenocarcinoma: correlation with histologic pattern and direction of spread. Am J Surg Pathol 1988;12(12):897–906.

18. Ayala AG, Ro JY, Babaian R, Troncoso P, Grignon DJ. The prostatic capsule: does it exist? Its importance in the staging and treatment of prostatic carcinoma. Am J Surg Pathol 1989;13(1):21–27.
19. Epstein JI. An update of the Gleason grading system. J Urol 2010;183(2):433–440.
20. Makarov DV, Sanderson H, Partin AW, Epstein JI. Gleason score 7 prostate cancer on needle biopsy: is the prognostic difference in Gleason scores 4 + 3 and 3 + 4 independent of the number of involved cores? J Urol 2002;167(6):2440–2442.
21. Kang DE, Fitzsimons NJ, Presti JC Jr, et al. Risk stratification of men with Gleason score 7 to 10 tumors by primary and secondary Gleason score: results from the SEARCH database. Urology 2007;70 (2):277–282.
22. Bezzi M, Kressel HY, Allen KS, et al. Prostatic carcinoma: staging with MR imaging at 1.5 T. Radiology 1988;169(2):339–346.
23. Hricak H, Choyke PL, Eberhardt SC, Leibel SA, Scardino PT. Imaging prostate cancer: a multidisciplinary perspective. Radiology 2007;243(1):28–53.
24. Yu KK, Hricak H, Alagappan R, Chernoff DM, Bacchetti P, Zaloudek CJ. Detection of extracapsular extension of prostate carcinoma with endorectal and phased-array coil MR imaging: multivariate feature analysis. Radiology 1997;202(3):697–702.
25. Bonekamp D, Macura KJ. Dynamic contrast-enhanced magnetic resonance imaging in the evaluation of the prostate. Top Magn Reson Imaging 2008;19 (6):273–284.
26. Moseley ME, Kucharczyk J, Mintorovitch J, et al. Diffusion-weighted MR imaging of acute stroke: correlation with T2-weighted and magnetic susceptibility-enhanced MR imaging in cats. AJNR Am J Neuroradiol 1990;11(3):423–429.
27. Hosseinzadeh K, Schwarz SD. Endorectal diffusion-weighted imaging in prostate cancer to differentiate malignant and benign peripheral zone tissue. J Magn Reson Imaging 2004;20(4):654–661.
28. Haider MA, van der Kwast TH, Tanguay J, et al. Combined T2-weighted and diffusion-weighted MRI for localization of prostate cancer. AJR Am J Roentgenol 2007;189(2):323–328.
29. desouza NM, Reinsberg SA, Scurr ED, Brewster JM, Payne GS. Magnetic resonance imaging in prostate cancer: the value of apparent diffusion coefficients for identifying malignant nodules. Br J Radiol 2007;80(950):90–95.
30. Le Bihan D, Breton E, Lallemand D, Grenier P, Cabanis E, Laval-Jeantet M. MR imaging of intravoxel incoherent motions: application to diffusion and perfusion in neurologic disorders. Radiology 1986;161(2):401–407.
31. Tamada T, Sone T, Jo Y, et al. Apparent diffusion coefficient values in peripheral and transition zones of the prostate: comparison between normal and malignant prostatic tissues and correlation with histologic grade. J Magn Reson Imaging 2008;28(3): 720–726.
32. Rosenkrantz AB, Kopec M, Kong X, et al. Prostate cancer vs. post-biopsy hemorrhage: diagnosis with T2- and diffusion-weighted imaging. J Magn Reson Imaging 2010;31(6):1387–1394.
33. Kim JH, Kim JK, Park BW, Kim N, Cho KS. Apparent diffusion coefficient: prostate cancer versus noncancerous tissue according to anatomical region. J Magn Reson Imaging 2008;28(5):1173–1179.
34. Noworolski SM, Vigneron DB, Chen AP, Kurhanewicz J. Dynamic contrast-enhanced MRI and MR diffusion imaging to distinguish between glandular and stromal prostatic tissues. Magn Reson Imaging 2008;26(8):1071–1080.
35. Katahira K, Takahara T, Kwee TC, et al. Ultra-high-b-value diffusion-weighted MR imaging for the detection of prostate cancer: evaluation in 201 cases with histopathological correlation. Eur Radiol 2011; 21(1):188–196.
36. Kim CK, Park BK, Kim B. High-b-value diffusion-weighted imaging at 3 T to detect prostate cancer: comparisons between b values of 1,000 and 2,000 s/mm2. AJR Am J Roentgenol 2010;194(1): W33–W37.
37. Heerschap A, Jager GJ, van der Graaf M, Barentsz JO, Ruijs SHJ. Proton MR spectroscopy of the normal human prostate with an endorectal coil and a double spin-echo pulse sequence. Magn Reson Med 1997;37(2):204–213.
38. Yacoe ME, Sommer G, Peehl D. In vitro proton spectroscopy of normal and abnormal prostate. Magn Reson Med 1991;19(2):429–438.
39. Podo F. Tumour phospholipid metabolism. NMR Biomed 1999;12(7):413–439.
40. Shukla-Dave A, Hricak H, Eberhardt SC, et al. Chronic prostatitis: MR imaging and 1H MR spectroscopic imaging findings—initial observations. Radiology 2004;231(3):717–724.
41. Bottomley PA. Spatial localization in NMR spectroscopy in vivo. Ann N Y Acad Sci 1987;508: 333–348.
42. Jung JA, Coakley FV, Vigneron DB, et al. Prostate depiction at endorectal MR spectroscopic imaging: investigation of a standardized evaluation system. Radiology 2004;233(3):701–708.
43. Westphalen AC, Coakley FV, Kurhanewicz J, Reed G, Wang ZJ, Simko JP. Mucinous adenocarcinoma of the prostate: MRI and MR spectroscopy features. AJR Am J Roentgenol 2009;193(3):W238–W243.
44. Prando A, Billis A. Focal prostatic atrophy: mimicry of prostatic cancer on TRUS and 3D-MRSI studies. Abdom Imaging 2009;34(2):271–275.
45. van Dorsten FA, van der Graaf M, Engelbrecht MR, et al. Combined quantitative dynamic contrast-enhanced MR imaging and (1)H MR spectroscopic imaging of human prostate cancer. J Magn Reson Imaging 2004;20(2):279–287.
46. Coakley FV, Kurhanewicz J, Lu Y, et al. Prostate cancer tumor volume: measurement with endorectal MR and MR spectroscopic imaging. Radiology 2002;223(1):91–97.
47. Crehange G, Parfait S, Liegard M, et al. Tumor volume and metabolism of prostate cancer determined by proton magnetic resonance spectroscopic imaging at 3T without endorectal coil reveal poten-

tial clinical implications in the context of radiation oncology. Int J Radiat Oncol Biol Phys 2010 Jul 7. [Epub ahead of print]
48. Qayyum A, Coakley FV, Lu Y, et al. Organ-confined prostate cancer: effect of prior transrectal biopsy on endorectal MRI and MR spectroscopic imaging. AJR Am J Roentgenol 2004;183(4):1079–1083.
49. Kaji Y, Kurhanewicz J, Hricak H, et al. Localizing prostate cancer in the presence of postbiopsy changes on MR images: role of proton MR spectroscopic imaging. Radiology 1998;206(3):785–790.
50. Padhani AR, Harvey CJ, Cosgrove DO. Angiogenesis imaging in the management of prostate cancer. Nat Clin Pract Urol 2005;2(12):596–607.
51. Tofts PS, Brix G, Buckley DL, et al. Estimating kinetic parameters from dynamic contrast-enhanced T(1)-weighted MRI of a diffusable tracer: standardized quantities and symbols. J Magn Reson Imaging 1999;10(3):223–232.
52. Tofts PS. Modeling tracer kinetics in dynamic Gd-DTPA MR imaging. J Magn Reson Imaging 1997;7 (1):91–101.
53. Langer DL, van der Kwast TH, Evans AJ, Trachtenberg J, Wilson BC, Haider MA. Prostate cancer detection with multi-parametric MRI: logistic regression analysis of quantitative T2, diffusion-weighted imaging, and dynamic contrast-enhanced MRI. J Magn Reson Imaging 2009;30(2):327–334.
54. Kozlowski P, Chang SD, Jones EC, Berean KW, Chen H, Goldenberg SL. Combined diffusion-weighted and dynamic contrast-enhanced MRI for prostate cancer diagnosis: correlation with biopsy and histopathology. J Magn Reson Imaging 2006;24 (1):108–113.
55. Kurhanewicz J, Vigneron D, Carroll P, Coakley F. Multiparametric magnetic resonance imaging in prostate cancer: present and future. Curr Opin Urol 2008;18(1):71–77.
56. Alonzi R, Padhani AR, Allen C. Dynamic contrast enhanced MRI in prostate cancer. Eur J Radiol 2007;63(3):335–350.
57. Sciarra A, Panebianco V, Ciccariello M, et al. Magnetic resonance spectroscopic imaging (1H-MRSI) and dynamic contrast-enhanced magnetic resonance (DCE-MRI): pattern changes from inflammation to prostate cancer. Cancer Invest 2010;28(4):424–432.
58. Fütterer JJ, Engelbrecht MR, Huisman HJ, et al. Staging prostate cancer with dynamic contrast-enhanced endorectal MR imaging prior to radical prostatectomy: experienced versus less experienced readers. Radiology 2005;237(2):541–549.
59. Sciarra A, Panebianco V, Ciccariello M, et al. Value of magnetic resonance spectroscopy imaging and dynamic contrast-enhanced imaging for detecting prostate cancer foci in men with prior negative biopsy. Clin Cancer Res 2010;16(6):1875–1883.
60. Franiel T, Lüdemann L, Rudolph B, et al. Evaluation of normal prostate tissue, chronic prostatitis, and prostate cancer by quantitative perfusion analysis using a dynamic contrast-enhanced inversion-prepared dual-contrast gradient echo sequence. Invest Radiol 2008;43(7):481–487.
61. Fütterer JJ, Scheenen TW, Huisman HJ, et al. Initial experience of 3 tesla endorectal coil magnetic resonance imaging and 1H-spectroscopic imaging of the prostate. Invest Radiol 2004;39(11):671–680.
62. Sosna J, Pedrosa I, Dewolf WC, Mahallati H, Lenkinski RE, Rofsky NM. MR imaging of the prostate at 3 Tesla: comparison of an external phased-array coil to imaging with an endorectal coil at 1.5 Tesla. Acad Radiol 2004;11(8):857–862.
63. Heijmink SW, Fütterer JJ, Hambrock T, et al. Prostate cancer: body-array versus endorectal coil MR imaging at 3 T—comparison of image quality, localization, and staging performance. Radiology 2007; 244(1):184–195.
64. Hamilton G, Middleton MS, Choi SH, Salibi N, Mattrey RF. Improved MR spectral analysis for a PFC-filled endorectal prostate surface coil compared to an air-filled coil [abstr]. In: Proceedings of the 15th Meeting of the International Society for Magnetic Resonance in Medicine. Berkeley, Calif: International Society for Magnetic Resonance in Medicine, 2007; 293.
65. Chen AP, Xu D, Sotto C, Coakley FV, Kurhanewicz J, Vigneron DB. High resolution MRSI and DTI of prostate cancer at 3T [abstr]. In: Proceedings of the 15th Meeting of the International Society for Magnetic Resonance in Medicine. Berkeley, Calif: International Society for Magnetic Resonance in Medicine, 2007; 558.
66. Barker PB, Hearshen DO, Boska MD. Single-voxel proton MRS of the human brain at 1.5T and 3.0T. Magn Reson Med 2001;45(5):765–769.
67. Sodickson DK, Manning WJ. Simultaneous acquisition of spatial harmonics (SMASH): fast imaging with radiofrequency coil arrays. Magn Reson Med 1997;38(4):591–603.
68. Gibbs P, Pickles MD, Turnbull LW. Diffusion imaging of the prostate at 3.0 tesla. Invest Radiol 2006; 41(2):185–188.
69. Heisen M, Fan X, Buurman J, van Riel NA, Karczmar GS, ter Haar Romeny BM. The influence of temporal resolution in determining pharmacokinetic parameters from DCE-MRI data. Magn Reson Med 2010;63(3):811–816.
70. Turkbey B, Pinto PA, Mani H, et al. Prostate cancer: value of multiparametric MR imaging at 3 T for detection—histopathologic correlation. Radiology 2010;255(1):89–99.
71. Ukimura O, Gill IS. Image-fusion, augmented reality, and predictive surgical navigation. Urol Clin North Am 2009;36(2):115–123.
72. Susil RC, Ménard C, Krieger A, et al. Transrectal prostate biopsy and fiducial marker placement in a standard 1.5T magnetic resonance imaging scanner. J Urol 2006;175(1):113–120.
73. Lattouf JB, Grubb RL 3rd, Lee SJ, et al. Magnetic resonance imaging-directed transrectal ultrasonography-guided biopsies in patients at risk of prostate cancer. BJU Int 2007;99(5):1041–1046.
74. Futterer JJ, Schouten M, Scheenen TW, Barentsz J. MR-compatible transrectal prostate biopsy robot: a feasibility study [abstr]. In: Proceedings of the 18th Meeting of the International Society for Magnetic Resonance in Medicine. Berkeley, Calif: International Society for Magnetic Resonance in Medicine, 2010.
75. Stoianovici D, Song D, Petrisor D, et al. "MRI Stealth" robot for prostate interventions. Minim Invasive Ther Allied Technol 2007;16(4):241–248.

# Advancements in MR Imaging of the Prostate: From Diagnosis to Interventions

*David Bonekamp, MD, PhD • Michael A. Jacobs, PhD • Riham El-Khouli, MD • Dan Stoianovici, PhD • Katarzyna J. Macura, MD, PhD*

**RadioGraphics 2011;** 31:677–703 • **Published online** 10.1148/rg.313105139 • **Content Codes:** US MR CT

**Page 679**
Currently, prostate cancer screening is based on assessment of the level of PSA elevation and results of digital rectal examination (DRE). Both markers have suboptimal accuracy for the diagnosis of prostate cancer.

**Page 682**
In the axial plane, the prostate is divided into four zones: *(a)* the anterior fibromuscular stroma, which contains no glandular tissue; *(b)* the transition zone surrounding the urethra, which contains 5% of the glandular tissue; *(c)* the central zone, which contains 20% of the glandular tissue; and *(d)* the outer peripheral zone, which contains 70%–80% of the glandular tissue (17).

**Page 689**
Reduced diffusion of water in prostate cancer has been attributed to the increased cellularity of malignant lesions, with reduction of the extracellular space and restriction of the motion of a larger portion of water molecules to the intracellular space. Therefore, diffusion-weighted imaging provides an important quantitative biophysical parameter that can be used to differentiate benign from malignant prostate tissue (27).

**Page 693**
An increase in the choline-to-citrate ratio or the (choline + creatine)/citrate ratio is often used as a marker of malignancy in prostate cancer and increases the specificity of diagnosis; however, it is most reliable in the peripheral zone.

**Page 694**
In prostate cancer, increased tumor vascularity leads to early hyperenhancement (higher and earlier peak enhancement than in normal tissue) and to rapid washout of contrast material from the tumor, in comparison with normal prostate tissue (Fig 4). Microvascular alterations and neovascularity are in general most severe in prostate cancer, in comparison with other processes in the prostate such as BPH or prostatic intraepithelial neoplasia (50).